

Non-iterative complex variable solution on sequential shallow tunnelling in gravitational geomaterial with reasonable far-field displacement

Luo-bin Lin^a, Fu-quan Chen^{b,*}, Change-jie Zheng^a, Shang-shun Lin^a

^a*Fujian Provincial Key Laboratory of Advanced Technology and Informatization in Civil Engineering, College of Civil Engineering, Fujian University of Technology, No. 69 Xueyuan Road, Shangjie University Town, Fuzhou, 350118, Fujian, China*

^b*College of Civil Engineering, Fuzhou University, No. 2 Xueyuan Road, Shangjie University Town, Fuzhou, 350108, Fujian, China*

Abstract

Sequential excavation is common in shallow tunnel engineering, especially for large-span tunnels. However, existing complex variable solutions can not handle sequential shallow tunnelling effectively. This paper proposes a new complex variable solution on sequential shallow tunnelling in gravitational geomaterial with reasonable far-field displacement in a non-iterative manner by incorporating a bidirectional stepwise conformal mapping combining Charge Simulation Method and Complex Dipole Simulation Method. The non-iterative manner ensures that the mechanical models of sequential excavation stages share similar mathematical formation with non-successive mixed boundary conditions, which are respectively transformed into corresponding homogeneous Riemann-Hilbert problems, and are solved to obtain stress and displacement fields of sequential shallow tunnelling. The proposed solution is subsequently validated by sufficient comparisons with equivalent finite element solution with good agreements. The comparisons also suggest that the proposed solution should be more accurate than the finite element one. A parametric investigation is finally conducted to illustrate possible practical applications of the proposed solution with several engineering recommendations. Additionally, the theoretical improvements and defects of the proposed solution are discussed for objectivity.

Keywords:

Sequential shallow tunnelling, Complex variable method, Non-iterative formation, Far-field displacement, Bidirectional conformal mapping

1. Introduction

Sequential excavation is a widely used and effective construction method in large-span tunnels, for example, the Niayesh Road Tunnel of Niayesh and Sadr highways in Tehran [1], the typical loess tunnel of the Zhengzhou-Xi'an high-speed railway [2], the Hejie Tunnel of the Guiyang-Guangzhou high-speed railway [3], the Yingpan Road Tunnel in Changsha [4], the Laodongshan Tunnel of the Guangtong-Kunming high-speed railway [5], the Lianchengshan Tunnel of the Yinchuan-Kunming National Expressway [6], the Laohushan Tunnel of the Jinan Ring Expressway [7]. According to excavation sequence, the construction methods can be classified into several categories, such as

*Corresponding author

Email addresses: luobin_lin@fjut.edu.cn (Luo-bin Lin), phdchen@fzu.edu.cn (Fu-quan Chen), zcj@fjut.edu.cn (Change-jie Zheng), linshangshun@fjut.edu.cn (Shang-shun Lin)

side drift method, center diagram method, top heading and bench method, upper half vertical subdivision method, and so on. Fig. 1 shows typical side drift and center diagram schemes, and is cited from Ref [1]. These sequential excavation methods are well investigated using numerical methods (finite element method and finite difference method for instance) incorporating above case studies [2, 3, 4, 6, 7], in which the ground surface is generally considered to meet the engineering facts.

Though the numerical methods would deliver satisfactory results of sequential tunnelling with consideration of ground surface (in other word, sequential shallow tunnelling), several potential defects exist: (1) Long runtime of numerical models, especially for a full parametric analysis; (2) Multiple modellings for relevant sequential shallow tunnelling of different but similar geometries; and (3) Possible license deficiency of necessary commercial numerical softwares (ABAQUS and FLAC for instance). By contrast, analytical methods, such as complex variable method, can be used to adapt the above-mentioned potential defects of the numerical methods in the preliminary design stage of sequential shallow tunnelling.

The most classical complex variable solution on shallow tunnelling is the Verruijt solution [8, 9], in which the Verruijt conformal mapping is proposed to bidirectionally map a lower half plane containing a circular cavity onto a unit annulus. Based on the Verruijt conformal mapping, several extending solutions are developed to estimate the traction along circular cavity boundary [10, 11, 12, 13], to simulate the displacement along circular cavity boundary [14, 15, 16], and to apply ground surface traction [17, 18, 19, 16]. However, no gravitational gradient of geomaterial is considered in the above extending solutions, which is a significant mechanical feature to distinguish shallow tunnelling from deep tunnelling. Strack [20] proposed the first complex variable solution on shallow tunnelling with consideration of gravitational gradient of geomaterial using Verruijt conformal mapping, and more relevant studies followed [21, 22, 23, 24, 25]. The complex variable solutions mentioned above all focus on circular shallow tunnelling, while noncircular tunnels are also widely used in real-world engineering.

To adapt noncircular shallow tunnelling, Zeng et al. [26] proposed an extension of Verruijt conformal mapping by adding finite items in formation of bilateral Laurent series to backwardly map a unit annulus onto a lower half plane containing a noncircular but symmetrical cavity, and more complex variable solutions on noncircular shallow tunnelling by consideration of gravitational gradient are proposed [27, 28, 29, 30, 31]. The above complex variable solutions on noncircular shallow tunnelling are incapable of dealing with the displacement singularity at infinity caused by unbalanced resultant due to excavation of gravitational geomaterial. To cope with the displacement singularity at infinity, new mechanical models are established by constraining far-field ground surface to artificially generate necessary constraining force to equilibrate the unbalanced resultant due to excavation [32, 33, 34, 35].

The brief literature review on complex variable method of shallow tunnelling indicates a deficiency of complex variable solution on sequential shallow tunnelling, which is commonly used in the many tunnelling cases mentioned above [1, 2, 3, 4, 6, 7], and thereby has theoretical and real-world engineering value to investigate. In this paper, we seek a complex variable solution on sequential shallow tunnelling with variety of cavity shape change in a gravitational geomaterial, and displacement singularity at infinity caused by sequential excavation should be eliminated simultaneously to reach reasonable stress and displacement fields.

This paper is organized as follows. Section 2 defines unified notations of geometrical variations and mathematically describes sequential shallow tunnelling in unsolvable iterative and solvable non-iterative formations with respective mixed boundary conditions. Section 3 transforms mixed boundary conditions of the solvable non-iterative formation of sequential shallow tunnelling into

corresponding homogeneous Riemann-Hilbert problems, and provides suitable bidirectional conformal mapping and stable solution procedure to reach stress and displacement fields. Section 4 illustrates detailed validation of proposed solution by sufficient comparisons with finite element solution. Section 5 conducts a parametric investigation to discuss several significant indexes of sequential shallow tunnelling. Section 6 makes further discussions on the theoretical improvements and several defects of the present solution for objectivity.

2. Typical sequential shallow tunnelling

2.1. Geometrical variations and notations

We may start from a gravitational geomaterial in Fig. 2a. The ground surface is denoted by \mathbf{C}_0 , the geomaterial region is denoted by $\mathbf{\Omega}_0$, and the closure $\overline{\mathbf{\Omega}}_0 = \mathbf{C}_0 \cup \mathbf{\Omega}$. The violet dash line denotes the possible final cavity boundary to be excavated. Two possible sequential shallow tunnelling schemes different from Fig. 1 are shown in Figs. 2b and 2c.

Fig. 2b shows one possible excavation scheme using top heading and bench method, in which the light cyan regions denote the to-be-excavated regions in different excavation stages, the violet solid lines denote cavity boundaries that would not be altered in present excavation stages, orange dash lines denote the intersection lines between excavated regions and to-be-excavated regions. Fig. 2b shows that the cavity is excavated from top to bottom stepwisely, and no temporary supports may be needed. However, the symmetrically noncircular cavity geometry of top-heading-bench method in Fig. 2b can already be mathematically studied by existing conformal mappings and complex variable solutions in above mentioned Refs [26, 27, 28, 29, 30, 31], and no obvious mathematical improvements of conformal mapping and complex variable method are thereby necessary.

By contrast, cavity geometry of the multi-stepwise upper half vertical subdivision method in Fig. 2c would no longer hold symmetry, and the existing conformal mappings and complex variable solutions in Refs [26, 27, 28, 29, 30, 31] would fail, and new conformal mapping scheme should be developed to form corresponding complex variable solution. The four-stage excavation scheme in Fig. 2c is only a possible example of sequential shallow tunnelling for visualized illustration. Practical excavation schemes may be more complicated in real-world tunnel engineering, and temporary supports are generally needed. In this paper, we would focus on the mechanical variation of gravitational geomaterial alone caused by multi-stepwise upper half vertical subdivision method, and temporary supports are not considered.

To adapt the real-world complicated excavation schemes, we should use abstract notations to present possible excavation schemes in the following notations. A sequential shallow tunnelling is decomposed into N stages. The excavated region and to-be-excavated region for j^{th} stage ($j = 1, 2, 3, \dots, N$) are denoted by \mathbf{D}_{j-1} and $\mathbf{D}_{j-1,j}$, whose boundaries are denoted by \mathbf{C}_j and $\mathbf{C}_{j-1,j}$, respectively. The intersection line between regions \mathbf{D}_j and $\mathbf{D}_{j-1,j}$ is denoted by $\mathbf{E}_{j-1,j}$. The above notations of regions and cavity boundaries are abstracted from Figs. 2b and 2c. When $j = 1$, the excavated region $\mathbf{D}_0 = \emptyset$ denotes no excavation has been conducted before 1st stage, and $\mathbf{E}_{0,1} = \mathbf{D}_0 \cap \mathbf{D}_{0,1} = \emptyset$. After j^{th} excavation, the remaining geomaterial region is reduced as a closure $\overline{\mathbf{\Omega}}_j = \overline{\mathbf{\Omega}}_0 - \mathbf{D}_j$. As shown in Fig. 2c, for each stage, the excavated region after j^{th} excavation always remains simply-connected, so that the rest geomaterial region $\overline{\mathbf{\Omega}}_j$ after j^{th} excavation should always remain doubly-connected to hold the consistent connectivity and topology. With the above notations, the regions and cavity boundaries of adjacent excavation stages can be computed in the following Boolean operation as

$$\mathbf{D}_j = \mathbf{D}_{j-1} \cup \mathbf{D}_{j-1,j} \cup \mathbf{E}_{j-1,j} \quad (2.1a)$$

$$\mathbf{C}_j = \tilde{\mathbf{C}}_{j-1} \cup \tilde{\mathbf{C}}_{j-1,j} \quad (2.1b)$$

where $\tilde{\mathbf{C}}_{j-1} = \mathbf{C}_{j-1} - \mathbf{E}_{j-1,j}$, $\tilde{\mathbf{C}}_{j-1,j} = \mathbf{C}_{j-1,j} - \mathbf{E}_{j-1,j}$, $j = 1, 2, 3, \dots, N$. The rest geomaterial $\mathbf{\Omega}_j = \mathbf{\Omega}_0 - \mathbf{D}_j$ should always hold double connectivity for topological consistence.

2.2. Initial stress field and mechanical properties of geomaterial

As shown in Fig. 2a, the geomaterial occupying the lower half plane $\overline{\mathbf{\Omega}}_0$ is assumed to be of small deformation with elasticity E , Poisson's ratio ν , and shear modulus of $G = \frac{E}{2(1+\nu)}$. A complex rectangular coordinate system $z = x + iy$ locating at some point of the ground surface \mathbf{C}_0 . An initial stress field of gravitational gradient γ and lateral coefficient k_x is orthotropically subjected through the geomaterial as

$$\begin{cases} \sigma_x^0(z) = k_x \gamma y \\ \sigma_y^0(z) = \gamma y \\ \tau_{xy}^0(z) = 0 \end{cases}, \quad z = x + iy \in \overline{\mathbf{\Omega}}_0 \quad (2.2)$$

where σ_x^0 , σ_y^0 , and τ_{xy}^0 denote horizontal, vertical, and shear components of the initial stress field, respectively. Before excavation, the displacement in geomaterial is artificially reset to be zero.

2.3. Sequential excavation in iterative formation and its limits

Before j^{th} ($j = 1, 2, 3, \dots, n$) excavation stage, the surface traction along to-be-excavated boundary $\tilde{\mathbf{C}}_{j-1,j}$ can be expressed as

$$\begin{cases} X_b^{j-1,j}(S_j) = \sigma_x^{j-1}(S_j) \cdot \cos\langle \vec{n}_j, \vec{x} \rangle + \tau_{xy}^{j-1}(S_j) \cdot \cos\langle \vec{n}_j, \vec{y} \rangle \\ Y_b^{j-1,j}(S_j) = \tau_{xy}^{j-1}(S_j) \cdot \cos\langle \vec{n}_j, \vec{x} \rangle + \sigma_y^{j-1}(S_j) \cdot \cos\langle \vec{n}_j, \vec{y} \rangle \end{cases}, \quad S_j \in \tilde{\mathbf{C}}_{j-1,j} \quad (2.3)$$

where $X_b^{j-1,j}$ and $Y_b^{j-1,j}$ denote horizontal and vertical components of surface traction along cavity boundary $\tilde{\mathbf{C}}_j$ before j^{th} excavation stage, respectively; σ_x^{j-1} , σ_y^{j-1} , and τ_{xy}^{j-1} denote horizontal, vertical, and shear components after $(j-1)^{\text{th}}$ excavation, respectively; S_j is an arbitrary point along first-stage cavity boundary \mathbf{C}_j ($\tilde{\mathbf{C}}_{j-1,j} \subset \mathbf{C}_j$); \vec{n}_j denotes the outward normal along cavity boundary \mathbf{C}_j , which always point towards the inside of \mathbf{C}_j ; $\langle \vec{n}_j, \vec{x} \rangle$ denotes the angle between outward normal \vec{n}_j and x axis, and $\langle \vec{n}_j, \vec{y} \rangle$ denotes the angle between outward normal \vec{n}_j and y axis.

To conduct j^{th} excavation, the following opposite surface traction is applied the along to-be-excavated cavity boundary $\tilde{\mathbf{C}}_{j-1,j}$ as

$$X_a^{j-1,j}(S_j) + iY_a^{j-1,j}(S_j) = - \left[X_b^{j-1,j}(S_j) + iY_b^{j-1,j}(S_j) \right], \quad S_j \in \tilde{\mathbf{C}}_{j-1,j} \quad (2.4a)$$

Meanwhile, the geomaterial is reduced from $\overline{\mathbf{\Omega}}_{j-1}$ to $\overline{\mathbf{\Omega}}_j = \overline{\mathbf{\Omega}}_{j-1} - \mathbf{D}_j - \mathbf{E}_{j-1,j}$. The sum of Eqs. (2.3) and (2.4a) would turn the tractions along cavity boundary $\tilde{\mathbf{C}}_{j-1,j}$ to zero in theory. Meanwhile, the rest cavity boundary $\tilde{\mathbf{C}}_{j-1}$ is free, so that the surface traction can be expressed as

$$X_a^{j-1,j}(S_j) + iY_a^{j-1,j}(S_j) = 0, \quad S_j \in \tilde{\mathbf{C}}_{j-1} \quad (2.4b)$$

where $X_a^{j-1,j}$ and $Y_a^{j-1,j}$ denote horizontal and vertical components of opposite surface traction along cavity boundary $\tilde{\mathbf{C}}_j$ after j^{th} excavation, respectively.

The nonzero resultant of opposite surface tractions $X_a^{j-1,j}$ and $Y_a^{j-1,j}$ along cavity boundary $\tilde{\mathbf{C}}_{j-1,j}$ can be computed as

$$R_{j-1,j} = \int_{\tilde{\mathbf{C}}_{j-1,j}} [X_a^{j-1,j}(S_j) + iY_a^{j-1,j}(S_j)] dS_j \quad (2.5)$$

The resultant $R_{j-1,j}$ should be located at point $z_{j-1,j}^c$ within region $\mathbf{D}_{j-1,j}$. To equilibriate the nonzero resultant $R_{j-1,j}$, the far-field ground surface \mathbf{C}_{0c} is constrained (without both joint points T_1 and T_2), while the rest finite ground surface \mathbf{C}_{0f} is left free (without both joint points T_1 and T_2), so that the follow equilibrium and boundary conditions along ground surface can be established as

$$\int_{\mathbf{C}_{0c}} [X_{jc}(T) + iY_{jc}(T)] dT = -R_{j-1,j}, \quad T \in \mathbf{C}_{0c} \quad (2.6)$$

$$u_c^{j-1,j}(T) + iv_c^{j-1,j}(T) = 0, \quad T \in \mathbf{C}_{0c} \quad (2.7a)$$

$$X_f^{j-1,j}(T) + iY_f^{j-1,j}(T) = 0, \quad T \in \mathbf{C}_{0f} \quad (2.7b)$$

where $X_c^{j-1,j}$ and $Y_c^{j-1,j}$ denote horizontal and vertical components of surface traction along the constrained ground surface \mathbf{C}_{0c} due to j^{th} -stage excavation, respectively; $u_c^{j-1,j}$ and $v_c^{j-1,j}$ denote horizontal and vertical components of displacement along the constrained ground surface \mathbf{C}_{0c} due to j^{th} -stage excavation, respectively; $X_f^{j-1,j}$ and $Y_f^{j-1,j}$ denote horizontal and vertical components of surface traction along the finite free ground surface due to j^{th} -stage excavation, respectively; T denotes arbitrary point along ground surface; the joint points of ground segments \mathbf{C}_{0c} and \mathbf{C}_{0f} are denoted by T_1 and T_2 , whose coordinates are fixed as $(-x_0, 0)$ and $(x_0, 0)$, respectively. We should emphasize that both joint points T_1 and T_2 are not included in boundary \mathbf{C}_{0c} or \mathbf{C}_{0f} , and would be singularities in theory due to the sudden change of boundary conditions in Eqs. (2.7a) and (2.7b). In other words, the geomaterial region can be expressed as $\bar{\Omega}_j = \Omega_j \cup \mathbf{C}_{0c} \cup \mathbf{C}_{0f} \cup \{T_1, T_2\}$.

The surface traction and equilibrium in Eqs. (2.3)-(2.7) are abstract, thus, we present an example in Fig. 3 for auxiliary illustration. Fig. 3 shows the geomaterial variation and boundary conditions of Stage-4 excavation of the example in Fig. 2c. Fig. 3a shows that (1) the geomaterial is $\bar{\Omega}_3$; (2) the surface tractions $X_b^{3,4}$ and $Y_b^{3,4}$ are applied along cavity boundary $\tilde{\mathbf{C}}_{3,4}$ before 4th-stage excavation; and (3) no surface traction is applied along cavity boundary $\tilde{\mathbf{C}}_3$. Fig. 3b geometrically shows that the geomaterial is reduced from $\bar{\Omega}_3$ to $\bar{\Omega}_4$, and that the infinite ground surface \mathbf{C}_{0c} is separated into a finite free segment \mathbf{C}_{0f} above cavity and the constrained far-field segment \mathbf{C}_{0c} with joint points T_1 and T_2 . The opposite surface tractions $X_a^{3,4}$ and $Y_a^{3,4}$ are applied along cavity boundary $\tilde{\mathbf{C}}_{3,4}$, and the resultant $R_{3,4}$ is located at point $z_{3,4}^c$ within the region $\mathbf{D}_{3,4}$. The cavity boundary $\tilde{\mathbf{C}}_3$ is still left free. The constrained ground surface \mathbf{C}_{0c} would provide constrained resultant in Eq. (2.6) to equilibriate the resultant $R_{3,4}$. The sum of surface tractions $X_b^{3,4}$ and $Y_b^{3,4}$ in Fig. 3a and opposite surface tractions $X_a^{3,4}$ and $Y_a^{3,4}$ in Fig. 3b would theoretically make cavity boundary $\tilde{\mathbf{C}}_4$ free from any surface traction, as discussed above.

Boundary conditions in Eqs. (2.4) and (2.7), as well as the static equilibrium in Eq. (2.6), would uniquely determine the mixed boundary conditions along j^{th} -stage excavation cavity boundary \mathbf{C}_j and ground surface \mathbf{C}_0 , respectively, so that the stress and displacement caused by j^{th} -stage excavation can be established as

$$\begin{cases} \sigma_y^{j-1,j}(z) + \sigma_x^{j-1,j}(z) = 2 [\varphi'_{j-1,j}(z) + \overline{\varphi'_{j-1,j}(z)}] \\ \sigma_y^{j-1,j}(z) - \sigma_x^{j-1,j}(z) + 2i\tau_{xy}^{j-1,j}(z) = 2 [\bar{z}\varphi''_{j-1,j}(z) + \psi'_{j-1,j}(z)] \end{cases}, \quad z \in \bar{\Omega}_j \setminus \{T_1, T_2\} \quad (2.8a)$$

$$2G [u_{j-1,j}(z) + iv_{j-1,j}(z)] = \kappa\varphi_{j-1,j}(z) - \overline{z\varphi'_{j-1,j}(z)} - \overline{\psi_{j-1,j}(z)}, \quad z \in \overline{\Omega}_j \setminus \{T_1, T_2\} \quad (2.8b)$$

where $\sigma_x^{j-1,j}$, $\sigma_y^{j-1,j}$, and $\tau_{xy}^{j-1,j}$ denote horizontal, vertical, and shear components of stress caused by j^{th} -stage excavation, respectively; $u_{j-1,j}$ and $v_{j-1,j}$ denote horizontal and vertical components of displacement caused by j^{th} -stage excavation, respectively; $\varphi_{j-1,j}$ and $\psi_{j-1,j}$ denote the complex potentials caused by the j^{th} -stage excavation, and can be uniquely determined by the mixed boundary conditions in Eqs. (2.4) and (2.7); $\kappa = 3 - 4\nu$ denotes the Kolosov parameter for plain strain. The total stress and displacement in geomaterial after j^{th} -stage excavation can be obtained as

$$\begin{cases} \sigma_x^j(z) = \sigma_x^{j-1}(z) + \sigma_x^{j-1,j}(z) \\ \sigma_y^j(z) = \sigma_y^{j-1}(z) + \sigma_y^{j-1,j}(z) \\ \tau_{xy}^j(z) = \tau_{xy}^{j-1}(z) + \tau_{xy}^{j-1,j}(z) \end{cases}, \quad z \in \overline{\Omega}_j \setminus \{T_1, T_2\} \quad (2.9a)$$

$$\begin{cases} u_j(z) = u_{j-1}(z) + u_{j-1,j}(z) \\ v_j(z) = v_{j-1}(z) + v_{j-1,j}(z) \end{cases}, \quad z \in \overline{\Omega}_j \setminus \{T_1, T_2\} \quad (2.9b)$$

where σ_x^j , σ_y^j , τ_{xy}^j denote horizontal, vertical, and shear components of total stress after j^{th} -stage excavation, respectively; u_j and v_j denote horizontal and vertical components of displacement after j^{th} -stage excavation, respectively. The zero displacement before excavation is defined as

$$\begin{cases} u_0(z) = 0 \\ v_0(z) = 0 \end{cases}, \quad z \in \overline{\Omega}_0 \quad (2.10)$$

Eq. (2.10) indicates that displacement before any excavation is reset to zero by consideration of geostress equilibrium due to initial stress field in Eq. (2.2).

For the next $(j + 1)^{\text{th}}$ -stage excavation, we should set $j : j + 1$ to continue the same procedure in Eqs. (2.3)-(2.9), until $j = N$ is reached. Mathematically, such a procedure is iteration. Therefore, the sequential shallow tunnelling can be described in iteration of Eqs. (2.3)-(2.9) by stepwisely increasing j from 1 to N , and the stress and displacement in Eq. (2.8) would overlap its previous iteration with sequential geometrical reduction of geomaterial from $\overline{\Omega}_0$ to $\overline{\Omega}_N$.

The above iterative sequential shallow tunnelling accords with stepwise excavation procedure in real-world engineering fact (temporary supports are not considered), and is concise in mathematical formation. However, a fatal defect exists that the boundary conditions along cavity boundary C_j in Eq. (2.4) and along ground surface C_0 in Eq. (2.7) are both mixed ones, while no existing solution technique has been explored for such mixed problem for both boundaries in complex variable method of geomechanical aspects. In other words, though the iterative mechanical procedure of sequential shallow tunnelling described in Eqs. (2.3)-(2.9) accords with real-world engineering fact (temporary supports are not considered) and our intuition, no solution can be obtained in present solution technique in complex variable method of geomechanics yet. Therefore, we should seek an alternative method for the same problem.

2.4. Alternative sequential excavation in non-iterative formation and its advantages

We may note that Eq. (2.9) can be rewritten by expanding the iterations as

$$\begin{cases} \sigma_x^j(z) = \sigma_x^0(z) + \sigma_x^{0,j}(z) \\ \sigma_y^j(z) = \sigma_y^0(z) + \sigma_y^{0,j}(z) \\ \tau_{xy}^j(z) = \tau_{xy}^0(z) + \tau_{xy}^{0,j}(z) \end{cases}, \quad z \in \overline{\Omega}_j \setminus \{T_1, T_2\}, 0 \leq j \leq N \quad (2.9a')$$

$$\begin{cases} u_j(z) = u_0(z) + u_{0,j}(z) \\ v_j(z) = v_0(z) + v_{0,j}(z) \end{cases}, \quad z \in \overline{\Omega}_j \setminus \{T_1, T_2\}, 0 \leq j \leq N \quad (2.9b')$$

with

$$\begin{cases} \sigma_x^{0,j}(z) = \sum_{l=1}^j \sigma_x^{l-1,l}(z) \\ \sigma_y^{0,j}(z) = \sum_{l=1}^j \sigma_y^{l-1,l}(z), \quad z \in \overline{\Omega}_j \setminus \{T_1, T_2\} \\ \tau_{xy}^{0,j}(z) = \sum_{l=1}^j \tau_{xy}^{l-1,l}(z) \end{cases} \quad (2.11a)$$

$$\begin{cases} u_{0,j}(z) = \sum_{l=1}^j u_{l-1,l}(z) \\ v_{0,j}(z) = \sum_{l=1}^j v_{l-1,l}(z) \end{cases}, \quad z \in \overline{\Omega}_j \setminus \{T_1, T_2\} \quad (2.11b)$$

where $\sigma_x^{0,j}$, $\sigma_y^{0,j}$, and $\tau_{xy}^{0,j}$ denote horizontal, vertical, and shear components of incremental stress field due to full excavation of \mathbf{D}_j geomaterial region from 0th stage to j^{th} stage, respectively; $u_{0,j}$ and $v_{0,j}$ denote horizontal and vertical components of incremental displacement field due to full excavation of \mathbf{D}_j geomaterial region from 0th stage to j^{th} stage, respectively. For simplicity, the range of $0 \leq j \leq N$ is not repeated in the following deductions.

Eqs. (2.9a') and (2.9b') show that the stress and displacement for j^{th} -stage excavation can be obtained by respectively summing up initial stress field and zero displacement of geostress equilibrium before excavation with incremental stress and displacement fields caused by full excavation of \mathbf{D}_j geomaterial region. In other words, the superposition principle is implicitly and reasonably used under the geomaterial assumption of elasticity and small deformation in Section 2.2.

With Eq. (2.11), the complex potentials in Eq. (2.8) can be reorganized as

$$\begin{cases} \sigma_y^{0,j}(z) + \sigma_x^{0,j}(z) = 2 [\varphi'_{0,j}(z) + \overline{\varphi'_{0,j}(z)}] \\ \sigma_y^{0,j}(z) - \sigma_x^{0,j}(z) + 2i\tau_{xy}^{0,j}(z) = 2 [\bar{z}\varphi''_{0,j}(z) + \psi'_{0,j}(z)] \end{cases}, \quad z \in \overline{\Omega}_j \setminus \{T_1, T_2\} \quad (2.12a)$$

$$2G[u_{0,j}(z) + iv_{0,j}(z)] = \kappa\varphi_{0,j}(z) - z\overline{\varphi'_{0,j}(z)} - \overline{\psi_{0,j}(z)}, \quad z \in \overline{\Omega}_j \setminus \{T_1, T_2\} \quad (2.12b)$$

where

$$\begin{cases} \varphi_{0,j}(z) = \sum_{l=1}^j \varphi_{l-1,l}(z) \\ \psi_{0,j}(z) = \sum_{l=1}^j \psi_{l-1,l}(z) \end{cases}, \quad z \in \overline{\Omega}_j \setminus \{T_1, T_2\} \quad (2.13)$$

The complex potentials in Eq. (2.12) are the sums of iterative complex potentials in Eq. (2.8) from 0th stage to j^{th} stage, therefore, the boundary conditions to solve the complex potentials in Eq. (2.12) should be different from those in Eqs. (2.4), (2.6), and (2.7), according to the uniqueness

theorem of complex variable method [36] and superposition principle. The traction along cavity boundary \mathbf{C}_j can be expressed as

$$\begin{cases} X_b^{0,j}(S_j) = \sigma_x^0(S_j) \cdot \cos\langle \vec{n}_j, \vec{x} \rangle + \tau_{xy}^0(S_j) \cdot \cos\langle \vec{n}_j, \vec{y} \rangle \\ Y_b^{0,j}(S_j) = \tau_{xy}^0(S_j) \cdot \cos\langle \vec{n}_j, \vec{x} \rangle + \sigma_y^0(S_j) \cdot \cos\langle \vec{n}_j, \vec{y} \rangle \end{cases}, \quad S_j \in \mathbf{C}_j \quad (2.14)$$

where $X_b^{0,j}$ and $Y_b^{0,j}$ denote horizontal and vertical components of surface traction of arbitrary point S_j along cavity boundary \mathbf{C}_j under the initial stress field from 0th stage to j^{th} stage, respectively.

Similar to Eq. (2.4a), the excavation after j^{th} stage is conducted by mechanically applying opposite surface traction of Eq. (2.14) along cavity boundary \mathbf{C}_j in the integral formation as

$$\int_{\mathbf{C}_j} [X_a^{0,j}(S_j) + iY_a^{0,j}(S_j)] dS_j = - \int_{\mathbf{C}_j} [X_b^{0,j}(S_j) + iY_b^{0,j}(S_j)] dS_j, \quad S_j \in \mathbf{C}_j \quad (2.15)$$

where $X_a^{0,j}$ and $Y_a^{0,j}$ denote horizontal and vertical components of opposite surface traction of arbitrary point S_j along cavity boundary \mathbf{C}_j under the initial stress field from 0th stage to j^{th} stage, respectively.

With the opposite surface traction in Eq. (2.15), the initial geomaterial $\overline{\Omega}_0$ is reduced to $\overline{\Omega}_j = \overline{\Omega}_0 - \mathbf{D}_j$. The nonzero resultant of surface traction in Eq. (2.15) can be given as

$$iR_y^{0,j} = \oint_{\mathbf{C}_j} [X_a^{0,j}(S_j) + iY_a^{0,j}(S_j)] dS_j = i\gamma \iint_{\mathbf{D}_j} dx dy \quad (2.16)$$

where the resultant is located as arbitrary point z_j^c within cavity boundary \mathbf{C}_j . It should be emphasized that the resultant $iR_y^{0,j}$ is always upward for $j = 1, 2, 3, \dots, N$ (which is clearly different from possibly non-upward $R_{j-1,j}$ in Eq. (2.5)), since the cavity boundary \mathbf{C}_j is closed and surrounds the simply-connected region \mathbf{D}_j , which is crossed through by the downward potential gravitational gradient γ .

The nonzero upward resultant should be equilibrated by constraining far-field ground surface \mathbf{C}_{0c} , and the following static equilibrium and mixed boundary conditions along ground surface can be established as

$$\int_{\mathbf{C}_{0c}} [X_a^{0,j}(T) + iY_a^{0,j}(T)] dT = -iR_y^{0,j}, \quad T \in \mathbf{C}_{0c} \quad (2.17)$$

$$u_c^{0,j}(T) + iv_c^{0,j}(T) = 0, \quad T \in \mathbf{C}_{0c} \quad (2.18a)$$

$$X_f^{0,j}(T) + iY_f^{0,j}(T) = 0, \quad T \in \mathbf{C}_{0f} \quad (2.18b)$$

where $u_c^{0,j}$ and $v_c^{0,j}$ denote horizontal and vertical components of displacement along ground surface segment \mathbf{C}_{0c} due to the excavation of geomaterial region \mathbf{D}_j from 0th stage to j^{th} stage, respectively; $X_f^{0,j}$ and $Y_f^{0,j}$ denote horizontal and vertical components of surface traction along ground surface segment \mathbf{C}_{0f} due to the excavation of geomaterial region \mathbf{D}_j from 0th stage to j^{th} stage, respectively. Eqs. (2.15) and (2.18) form the necessary boundary conditions for excavation of \mathbf{D}_j geomaterial region from 0th stage to j^{th} stage.

Fig. 4 present a corresponding case for graphic illustration of the abstract boundary conditions of non-iterative excavation scheme in this section using the example of Stage-4 excavation in Fig. 3. In Fig. 4a, the geomaterial region \mathbf{D}_4 is to be excavated, and the surface tractions along cavity boundary \mathbf{C}_4 before excavation caused by the initial stress field is denoted by $X_b^{0,4}$ and $Y_b^{0,4}$, while the rest parts are the same to the example in Fig. 3a. In Fig. 4b, the geomaterial region \mathbf{D}_4

is excavated, and the remaining geomaterial geometrically reduces from $\overline{\Omega}_0$ to $\overline{\Omega}_4 = \overline{\Omega}_0 - \mathbf{D}_4$. Meanwhile, the opposite surface tractions $X_a^{0,4}$ and $Y_a^{0,4}$ are applied along cavity boundary \mathbf{C}_4 . The upward resultant $R_y^{0,4}$ due to excavation of geomaterial region \mathbf{D}_4 is located at point z_4^c within cavity boundary \mathbf{C}_4 . The surface tractions $X_b^{0,4}$ and $Y_b^{0,4}$ in Fig. 4a and the opposite surface traction $X_a^{3,4}$ and $Y_a^{3,4}$ in Fig. 4b would cancel each other to free the boundary \mathbf{C}_4 .

With the mixed boundary conditions in Eqs. (2.15) and (2.18), and the static equilibrium in Eq. (2.17), the complex potentials, the stress and the displacement field in Eq. (2.12) can be uniquely determined. Then the stress and displacement of merely j^{th} -stage excavation can be obtained as

$$\begin{cases} \sigma_x^{j-1,j}(z) = \sigma_x^j(z) - \sigma_x^{j-1}(z) \\ \sigma_y^{j-1,j}(z) = \sigma_y^j(z) - \sigma_y^{j-1}(z) \\ \tau_{xy}^{j-1,j}(z) = \tau_{xy}^j(z) - \tau_{xy}^{j-1}(z) \end{cases}, \quad z \in \overline{\Omega}_j \setminus \{T_1, T_2\} \quad (2.19a)$$

$$\begin{cases} u_{j-1,j}(z) = u_j(z) - u_{j-1}(z) \\ v_{j-1,j}(z) = v_j(z) - v_{j-1}(z) \end{cases}, \quad z \in \overline{\Omega}_j \setminus \{T_1, T_2\} \quad (2.19b)$$

Note that the region relationship $\overline{\Omega}_j \subset \overline{\Omega}_{j-1}$ is always satisfied due to sequential excavation.

Eqs. (2.15), (2.17), and (2.18) show that the boundary conditions and static equilibrium always start from the initial stress field, instead of previous iterative stress field in Section 2.3, so that the complex potentials and the stress and displacement in Eq. (2.12) can be solved in non-iterative or parallel formation, instead of iterative or serial formation. Thus, the mathematical formation to solve stress and displacement due to excavation in this section is more stable with good fault tolerance.

More importantly, the boundary conditions in Eqs. (2.15) and (2.18), as well as the static equilibrium in Eq. (2.17), would form a Riemann-Hilbert problem with extra constraints [32, 34], which can be solved by an existing solution technique proposed in Refs [32, 34]. In other words, the mathematical formation in this section is solvable by existing solution technique, while the one in Section 2.3 is unsolvable for now.

3. Problem transformation and solution on sequential shallow tunnelling in non-iterative formation

In this section, the non-iterative complex variable method for sequential shallow tunnelling defined in Section 2.4 would be presented. To conduct the complex variable method, the physical geomaterial regions $\overline{\Omega}_j$ ($j = 1, 2, 3, \dots, N$) should be bidirectionally mapped onto corresponding mapping unit annuli $\overline{\omega}_j$ via suitable conformal mappings, so that the boundary conditions, complex potentials, stress and displacement within the physical geomaterial regions $\overline{\Omega}_j$ can be presented using the mathematically feasible Laurent series formations in the mapping unit annuli $\overline{\omega}_j$.

3.1. Riemann-Hilbert problem transformation

Our previous study [35] proposes a two-step conformal mapping scheme to bidirectionally map a lower half plane containing an arbitrary cavity onto a unit annulus. Each physical geomaterial region $\overline{\Omega}_j$ accords with the geometrical and topological requirements of the two-step conformal mapping in our previous study [35], and can be thereby bidirectionally mapped onto corresponding mapping unit annuli $\overline{\omega}_j$ as

$$\zeta_j = \zeta_j(z) = \zeta_j[w_j(z)], \quad z \in \overline{\Omega}_j \quad (3.1a)$$

$$z = z_j(\zeta_j) = z_j[w_j(\zeta_j)], \quad \zeta_j \in \overline{\omega}_j \quad (3.1b)$$

It should be emphasized that the variable z in Eq. (3.1) contains no subscript due to the reason that the subtractions in Eq. (2.19) require the stress and displacement being in the same coordinate system $z = x + iy$ for different physical geomaterial regions $\overline{\Omega}_j$. The mapping scheme in Eq. (3.1) is briefly explained in Appendix A. Via the bidirectional conformal mapping, the whole geomaterial in the lower half plane $\overline{\Omega}_j$ is bidirectionally mapped onto a bounded unit annulus $\overline{\omega}_j$; the cavity boundary \mathbf{C}_j is bidirectionally mapped onto the interior periphery of the unit annulus \mathbf{c}_j ; the constrained ground surface \mathbf{C}_{0c} and free one \mathbf{C}_{0f} are bidirectionally mapped onto corresponding segments $\mathbf{c}_{0c,j}$ and $\mathbf{c}_{0f,j}$ of exterior periphery of the unit annulus, respectively; the joint points T_1 and T_2 connecting \mathbf{C}_{0c} and \mathbf{C}_{0f} are bidirectionally mapped onto joint points $t_{1,j}$ and $t_{2,j}$ connecting $\mathbf{c}_{0c,j}$ and $\mathbf{c}_{0f,j}$, respectively. Joint points $t_{1,j}$ and $t_{2,j}$ in mapping region $\overline{\omega}_j$ should remain singularities after conformal mapping. We should emphasize that $\zeta_j = \rho_j \cdot \sigma_j = \rho_j \cdot e^{i\theta_j}$ holds in the following deductions.

With the conformal mapping scheme in Eq. (3.1), the complex potentials in Eq. (2.12) can be transformed as

$$\begin{cases} \varphi_{0,j}(z) = \varphi_{0,j}(\zeta_j) \\ \psi_{0,j}(z) = \psi_{0,j}(\zeta_j) \end{cases}, \quad \zeta_j \in \overline{\omega}_j \setminus \{t_{1,j}, t_{2,j}\} \quad (3.2)$$

Correspondingly, the stress and displacement in Eq. (2.12) can be expressed using polar formation as

$$\sigma_\theta^{0,j}(\zeta_j) + \sigma_\rho^{0,j}(\zeta_j) = 2 \left[\Phi_{0,j}(\zeta_j) + \overline{\Phi_{0,j}(\zeta_j)} \right], \quad \zeta_j \in \overline{\omega}_j \setminus \{t_{1,j}, t_{2,j}\} \quad (3.3a)$$

$$\sigma_\rho^{0,j}(\zeta_j) + i\tau_{\rho\theta}^{0,j}(\zeta_j) = \left[\Phi_{0,j}(\zeta_j) + \overline{\Phi_{0,j}(\zeta_j)} \right] - \frac{\overline{\zeta_j}}{\zeta_j} \left[\frac{z_j(\zeta_j)}{z_j'(\zeta_j)} \overline{\Phi_{0,j}'(\zeta_j)} + \frac{z_j'(\zeta_j)}{z_j(\zeta_j)} \overline{\Psi_{0,j}(\zeta_j)} \right], \quad \zeta_j \in \overline{\omega}_j \setminus \{t_{1,j}, t_{2,j}\} \quad (3.3b)$$

$$g_j(\zeta_j) = 2G [u_{0,j}(\zeta_j) + iv_{0,j}(\zeta_j)] = \kappa\varphi_{0,j}(\zeta_j) - z_j(\zeta_j)\overline{\Phi_{0,j}(\zeta_j)} - \overline{\psi_{0,j}(\zeta_j)}, \quad \zeta_j \in \overline{\omega}_j \setminus \{t_{1,j}, t_{2,j}\} \quad (3.3c)$$

where $\sigma_\theta^{0,j}$, $\sigma_\rho^{0,j}$, and $\tau_{\rho\theta}^{0,j}$ denote hoop, radial, and tangential components of the curvilinear stress mapped onto the mapping unit annuli $\overline{\omega}_j$, respectively; and

$$\begin{cases} \Phi_{0,j}(\zeta_j) = \frac{\varphi_{0,j}'(\zeta_j)}{z_j'(\zeta_j)} \\ \Psi_{0,j}(\zeta_j) = \frac{\psi_{0,j}'(\zeta_j)}{z_j'(\zeta_j)} \end{cases}, \quad \zeta_j \in \overline{\omega}_j \setminus \{t_{1,j}, t_{2,j}\}$$

The rectangular stress and displacement components in Eq. (2.12) can be computed using the curvilinear ones in Eq. (3.3) as

$$\begin{cases} \sigma_y^{0,j}(z) + \sigma_x^{0,j}(z) = \sigma_\theta^{0,j}[\zeta_j(z)] + \sigma_\rho^{0,j}[\zeta_j(z)] \\ \sigma_y^{0,j}(z) - \sigma_x^{0,j}(z) + 2i\tau_{xy}^{0,j}(z) = \left\{ \sigma_\theta^{0,j}[\zeta_j(z)] - \sigma_\rho^{0,j}[\zeta_j(z)] + 2i\tau_{\rho\theta}^{0,j}[\zeta_j(z)] \right\} \cdot \frac{\overline{\zeta_j(z)}}{\zeta_j(z)} \cdot \frac{z_j'[\zeta_j(z)]}{z_j[\zeta_j(z)]}, \quad z \in \overline{\Omega}_j \setminus \{T_1, T_2\} \end{cases} \quad (3.4a)$$

$$u_{0,j}(z) + iv_{0,j}(z) = u_{0,j}[\zeta_j(z)] + iv_{0,j}[\zeta_j(z)], \quad z \in \overline{\Omega}_j \setminus \{T_{1,j}, T_2\} \quad (3.4b)$$

With the conformal mapping scheme in Eq.(3.1), the mixed boundary conditions along ground surface in Eq. (2.18) can be mapped onto the mapping unit annuli $\overline{\omega}_j$ as

$$u_c^{0,j}(t_j) + iv_c^{0,j}(t_j) = 0, \quad t_j \in \mathbf{c}_{0c,j} \quad (3.5a)$$

$$\sigma_\rho^{0,j}(t_j) + i\tau_{\rho\theta}^{0,j}(t_j) = 0, \quad t_j \in \mathbf{c}_{0f,j} \quad (3.5b)$$

where $t_j = \sigma_j = e^{i\theta_j}$. Meanwhile, the surface traction along cavity boundary in Eq. (2.15) can also be mapped onto the mapping unit annuli $\bar{\omega}_j$.

The integrand of the left-hand side of Eq. (2.15) can be mapped from the physical plane $z = x + iy$ onto corresponding mapping plane $\zeta_j = \rho_j \cdot e^{i\theta_j}$ according to the backward conformal mapping in Eq. (3.1b) as

$$X_a^{0,j}(S_j) + iY_a^{0,j}(S_j) = \frac{z'_j(s_j)}{|z'_j(s_j)|} \frac{ds_j}{|ds_j|} \cdot [\sigma_\rho^{0,j}(s_j) + i\tau_{\rho\theta}^{0,j}(s_j)], \quad s_j \in \mathbf{c}_j \quad (3.6a)$$

where $s_j = \alpha_j \cdot \sigma_j = \alpha_j \cdot e^{i\theta_j}$, denoting the point along the mapping contour \mathbf{c}_j corresponding to the original point S_j along the physical contour \mathbf{C}_j . The integrand of the right-hand side of Eq. (2.15) can be expanded according to Eq. (2.14) as

$$X_b^{0,j}(S_j) + iY_b^{0,j}(S_j) = -k_x \gamma y(S_j) \frac{dy(S_j)}{dS_j} + i\gamma y(S_j) \frac{dy(S_j)}{dS_j}, \quad S_j \in \mathbf{C}_j \quad (3.6b)$$

where $\cos\langle \vec{n}_j, \vec{x} \rangle = \frac{dy}{dS_j}$ and $\cos\langle \vec{n}_j, \vec{y} \rangle = -\frac{dx}{dS_j}$ owing to the clockwise integrating direction. The increment dS_j in Eq. (2.15) is clockwise length increment with $dS_j = -|dS_j|$, which can be mapped from the physical plane $z = x + iy$ onto mapping plane $\zeta_j = \rho \cdot e^{i\theta_j}$ as

$$dS_j = -|dS_j| = -|z'_j(s_j)| \cdot |ds_j| = -|z'_j(s_j)| \cdot \alpha_j \cdot |\sigma_j| \cdot |d\theta_j| = |z'_j(s_j)| \cdot \alpha_j d\theta_j \quad (3.6c)$$

where $|d\theta_j| = -d\theta_j$, since conformal mapping would not alter the clockwise integration direction.

With Eq. (3.6a) and (3.6c), the left-hand side of Eq. (2.15) can be rearranged as

$$i \int_{\mathbf{C}_j} [X_a^{0,j}(S_j) + iY_a^{0,j}(S_j)] dS_j = \int_{\mathbf{c}_j} z'_j(s_j) [\sigma_\rho^{0,j}(s_j) + i\tau_{\rho\theta}^{0,j}(s_j)] \cdot \frac{|z'_j(s_j)|}{|z'_j(s_j)|} \cdot \alpha_j \cdot e^{i\theta_j} \cdot i \cdot d\theta_j \quad (3.7a)$$

where $ds_j = \alpha_j \cdot e^{i\theta_j} \cdot i \cdot d\theta_j$. With Eq. (3.6b), the right-hand side of Eq. (2.15) can be rearranged as

$$-i \int_{\mathbf{C}_j} [X_b^{0,j}(S_j) + iY_b^{0,j}(S_j)] dS_j = -\gamma \int_{\mathbf{C}_j} y(S_j) [k_x i dy(S_j) + dx(S_j)] \quad (3.7b)$$

Via the backward conformal mapping in Eq. (3.1b), the right-hand side of Eq. (3.7b) can be mapped as

$$\begin{cases} dy(S_j) = \frac{dy(s_j)}{d\sigma_j} d\sigma_j \\ dx(S_j) = \frac{dx(s_j)}{d\sigma_j} d\sigma_j \end{cases}$$

The right-hand sides of Eqs. (3.7a) and (3.7b) should be equal according to Eq. (2.15), and we should have

$$\int_{\mathbf{c}_j} z'_j(s_j) [\sigma_\rho^{0,j}(s_j) + i\tau_{\rho\theta}^{0,j}(s_j)] ds_j = -\gamma \int_{\mathbf{c}_j} y(s_j) \left[k_x \frac{idy(s_j)}{d\sigma_j} + \frac{dx(s_j)}{d\sigma_j} \right] d\sigma_j \quad (3.8)$$

where

$$\begin{cases} x(s_j) = \frac{1}{2} [\overline{z_j(s_j)} + z_j(s_j)] \\ y(s_j) = \frac{i}{2} [\overline{z_j(s_j)} - z_j(s_j)] \end{cases}$$

Eqs. (3.5) and (3.8) are the mixed boundary conditions mapped from Eqs. (2.18) and (2.15) into the mapping plane $\zeta_j = \rho_j \cdot e^{i\theta_j}$, respectively.

The segmental traction free boundary condition in Eq. (3.5b) can be used to establish analytic continuation and mixed boundary condition along ground surface regarding first-order derivative of complex potential $\Phi_{0,j}(\zeta_j)$. Substituting Eq. (3.3b) into Eq. (3.5b) yields

$$\overline{\Phi_{0,j}(t_j)} = -\Phi_{0,j}(t_j) + \frac{\bar{t}_j z_j(t_j)}{t_j z'_j(t_j)} \overline{\Phi'_{0,j}(t_j)} + \frac{\bar{t}_j \overline{z'_j(t_j)}}{t_j z'_j(t_j)} \overline{\Psi_{0,j}(t_j)}, \quad t_j \in \mathbf{c}_{0f,j} \quad (3.9)$$

Partially substituting $t_j = \bar{t}_j^{-1}$ into the items of the right-hand side of Eq. (3.9) yields

$$\overline{\Phi_{0,j}(t_j)} = -\Phi_{0,j}(\bar{t}_j^{-1}) + \frac{\bar{t}_j z_j(\bar{t}_j^{-1})}{\bar{t}_j^{-1} z'_j(\bar{t}_j^{-1})} \overline{\Phi'_{0,j}(t_j)} + \frac{\bar{t}_j \overline{z'_j(t_j)}}{\bar{t}_j^{-1} z'_j(\bar{t}_j^{-1})} \overline{\Psi_{0,j}(t_j)}, \quad t_j \in \mathbf{c}_{0f,j} \quad (3.10)$$

Replacing $t_j = \sigma_j$ with $\zeta_j = \rho_j \cdot \sigma_j$ in Eq. (3.10) yields

$$\overline{\Phi_{0,j}(\zeta_j)} = -\Phi_{0,j}(\bar{\zeta}_j^{-1}) + \bar{\zeta}_j \frac{z_j(\bar{\zeta}_j^{-1})}{z'_j(\bar{\zeta}_j^{-1})} \overline{\Phi'_{0,j}(\zeta_j)} + \bar{\zeta}_j \frac{\overline{z'_j(\zeta_j)}}{z'_j(\bar{\zeta}_j^{-1})} \overline{\Psi_{0,j}(\zeta_j)}, \quad \zeta_j \in \omega_j^+ \quad (3.11)$$

We should note that all items on the right-hand side of Eq. (3.11) are analytic in region $\alpha_j \leq \rho_j < 1$, which is contained within the exterior region ω_j^- . Thus, Eq. (3.11) shows that $\overline{\Phi_{0,j}(\zeta_j)}$ should be analytic in region $\alpha_j \leq \rho_j < 1$, indicating that analytic continuation has been conducted for $\overline{\Phi_{0,j}(\zeta_j)}$, or simply its conjugate $\Phi_{0,j}(\zeta_j)$.

Substituting Eq. (3.11) into Eq. (3.3b) yields

$$\begin{aligned} \sigma_\rho^{0,j}(\zeta_j) + i\tau_{\rho\theta}^{0,j}(\zeta_j) &= \bar{\zeta}_j^2 \left[\frac{z_j(\bar{\zeta}_j^{-1})}{z'_j(\bar{\zeta}_j^{-1})} - \frac{1}{\zeta_j \bar{\zeta}_j} \frac{z_j(\zeta_j)}{z'_j(\zeta_j)} \right] \overline{\Phi'_{0,j}(\zeta_j)} + \bar{\zeta}_j^2 \left[\frac{\overline{z'_j(\zeta_j)}}{z'_j(\bar{\zeta}_j^{-1})} - \frac{1}{\zeta_j \bar{\zeta}_j} \frac{\overline{z'_j(\zeta_j)}}{z'_j(\zeta_j)} \right] \overline{\Psi_j(\zeta_j)} \\ &\quad + \left[\Phi_{0,j}(\zeta_j) - \Phi_{0,j}(\bar{\zeta}_j^{-1}) \right], \quad \zeta_j \in \omega_j^+ \end{aligned} \quad (3.3b')$$

The first-order of Eq. (3.3c) about ζ_j can be expressed as

$$\frac{dg_j(\zeta_j)}{d\zeta_j} = \kappa z'_j(\zeta_j) \Phi_{0,j}(\zeta_j) - z'_j(\zeta_j) \overline{\Phi_{0,j}(\zeta_j)} + z_j(\zeta_j) \overline{\Phi'_{0,j}(\zeta_j)} + \frac{\bar{\zeta}_j}{\zeta_j} \overline{z'_j(\zeta_j)} \overline{\Psi_{0,j}(\zeta_j)} \quad (3.12)$$

Substituting Eq. (3.11) into Eq. (3.12) yields

$$\begin{aligned} \frac{dg_j(\zeta_j)}{d\zeta_j} &= \frac{\bar{\zeta}_j}{\zeta_j} \left[z_j(\zeta_j) - \zeta_j \bar{\zeta}_j \frac{z'_j(\zeta_j)}{z'_j(\bar{\zeta}_j^{-1})} z(\bar{\zeta}_j^{-1}) \right] \overline{\Phi'_{0,j}(\zeta_j)} + \frac{\bar{\zeta}_j}{\zeta_j} \left[\overline{z'_j(\zeta_j)} - \zeta_j \bar{\zeta}_j \frac{z'_j(\zeta_j)}{z'_j(\bar{\zeta}_j^{-1})} \overline{z'_j(\zeta_j)} \right] \overline{\Psi_{0,j}(\zeta_j)} \\ &\quad + \left[\kappa z'_j(\zeta_j) \Phi_{0,j}(\zeta_j) + z'_j(\zeta_j) \Phi_{0,j}(\bar{\zeta}_j^{-1}) \right], \quad \zeta_j \in \omega_j^+ \end{aligned} \quad (3.3c')$$

We should notice that when $\zeta_j \rightarrow \sigma_j$ (or $\rho_j \rightarrow 1$), the first lines of Eqs. (3.3b') and (3.3c') would turn to zero due to $\bar{\sigma}_j^{-1} = \sigma_j$, and remaining second lines would form a homogeneous Riemann-Hilbert problem as [32, 34, 35]

$$z'_j(\zeta_j) \left[\sigma_\rho^{0,j}(\zeta_j) + i\tau_{\rho\theta}^{0,j}(\zeta_j) \right] \Big|_{\rho_j \rightarrow 1} = \varphi_{0,j}^+(\sigma_j) - \varphi_{0,j}^-(\sigma_j) = 0, \quad \sigma_j \in \mathbf{c}_{0f,j} \quad (3.13a)$$

$$g'_j(\zeta_j)|_{\rho_j \rightarrow 1} = \kappa \varphi'_{0,j}^+(\sigma_j) + \varphi'_{0,j}^-(\sigma_j) = 0, \quad \sigma_j \in \mathbf{c}_{0c,j} \quad (3.13b)$$

where $\varphi'_{0,j}^+(\sigma_j)$ and $\varphi'_{0,j}^-(\sigma_j)$ denote the boundary values of $\varphi'_{0,j}(\zeta_j) = z'_j(\zeta_j)\Phi_{0,j}(\zeta_j)$ approaching boundary $\mathbf{c}_{0,j}$ from ω_j^+ and ω_j^- sides, respectively. Eqs. (3.13) and (3.8) would form a homogeneous Riemann-Hilbert problem with extra constraints, and the solution procedure would be briefly presented below.

3.2. Solution procedure of Riemann-Hilbert problem

Before any discussion of the solution, we should emphasize that all the discussion is conducted in the mapping plane $\zeta_j = \rho_j \cdot e^{i\theta_j}$. The general solution of the homogeneous Riemann-Hilbert problem in Eq. (3.13) can be given below. Eq. (3.13a) would be simultaneously satisfied owing to the analytic continuation of Eq. (3.11), and no further discussion should be needed. As for Eq. (3.13b), we construct the following expression to simulate one of its potential solutions as

$$X_j(\zeta_j) = (\zeta_j - t_{1,j})^{-\eta}(\zeta_j - t_{2,j})^{\eta-1}, \quad \zeta_j \in \bar{\omega}_j \cup \omega_j^- \setminus \{t_{1,j}, t_{2,j}\} \quad (3.14)$$

where $t_{1,j}$ and $t_{2,j}$ are the singularities mapped from T_1 and T_2 in the lower half geomaterial region $\bar{\Omega}_j$ via the bidirectional conformal mapping in Eq. (3.1), η denotes a complex coefficient to be determined. Eq. (3.14) can be reformulated by separation of the real and imaginary parts as

$$X_j(\zeta_j) = \exp \{ [-\eta \ln |\zeta_j - t_{1,j}| + (\eta - 1) \ln |\zeta_j - t_{2,j}|] \\ + i \cdot [-\eta \arg(\zeta_j - t_{1,j}) + (\eta - 1) \arg(\zeta_j - t_{2,j})] \}, \quad \zeta_j \in \bar{\omega}_j \cup \omega_j^- \setminus \{t_{1,j}, t_{2,j}\} \quad (*)$$

To confine Eq. (*) in the branch that satisfies $\lim_{\zeta_j \rightarrow \infty} \zeta_j X_j(\zeta_j) = 1$, we select the cut that starts from joint point $t_{1,j}$ with positive direction that sequentially connects the circular arc $\mathbf{c}_{0c,j}$ of fixed displacement (see Eq. (3.13b)) and joint point $t_{2,j}$, as well as complex infinity. The cut segment that starts from arc ending point $t_{2,j}$ to complex infinity can be denoted by $\mathbf{c}_{\infty,j}$. Thus, Eq. (3.14) would be analytic in the mapping plane $\zeta_j = \rho_j \cdot e^{i\theta_j}$ of the selected branch ($\lim_{\zeta_j \rightarrow \infty} \zeta_j X_j(\zeta_j) = 1$) with the cut $\{t_{1,j}\} \cup \mathbf{c}_{0c,j} \cup \{t_{2,j}\} \cup \mathbf{c}_{\infty,j}$.

Two possible patterns of the variation of variable ζ_j along the cut can be established to surround the singularities $t_{1,j}$ and $t_{2,j}$. For distinction, we use variable $\xi_j \in \mathbf{c}_{0c,j} \cup \mathbf{c}_{\infty,j}$, where points $t_{1,j}$ and $t_{2,j}$ are not included any more, because these two points are singularities to be surrounded. One possible pattern is $\xi_j \in \mathbf{c}_{\infty,j}$ with the contour fully surrounding the starting point $t_{1,j}$ for k times (k is an integer). On the left side of the cut, the imaginary part of $X_j^+(\xi_j)$ can be expressed according to Eq. (*) as

$$\arg X_j^+(\xi_j) = -\eta \arg(\xi_j - t_{1,j}) + (\eta - 1) \arg(\xi_j - t_{2,j}), \quad \xi_j \in \mathbf{c}_{\infty,j} \quad (3.15)$$

On the right side of the cut, surrounding of k times occurs, and the imaginary part of $X_j^-(\xi_j)$ can be expressed according to Eq. (*) as

$$\arg X_j^-(\xi_j) = -\eta [\arg(\xi_j - t_{1,j}) + 2k\pi] + (\eta - 1) [\arg(\xi_j - t_{2,j}) + 2k\pi] = \arg X_j^+(\xi_j) - 2k\pi, \quad \xi_j \in \mathbf{c}_{\infty,j} \quad (3.16a)$$

Combining the real part, Eq. (3.16a) would yield

$$X_j^+(\xi_j) - X_j^-(\xi_j) = 0, \quad \xi_j \in \mathbf{c}_{\infty,j} \quad (3.16a')$$

Eq. (3.16a') would hold due to $e^{-2k\pi i} = 1$. We should notice $\mathbf{c}_{\infty,j}$ is an arbitrary curve reaching complex infinity in Eq. (3.16a'), indicating that $X_j(\zeta_j)$ should be analytic within the whole mapping

plane $\zeta_j = \rho_j \cdot e^{i\theta_j}$, except for the cut segment $\mathbf{c}_{0c,j}$ and the singularities $t_{1,j}$ and $t_{2,j}$. Eq. (3.16a') matches the formation of Eq. (3.13a), which is always satisfied due to analytic continuation, and no further discussion is needed.

The other possible pattern is $\xi_j \in \mathbf{c}_{0c,j}$ with contour fully surrounding the start point $t_{1,j}$ for k times. It should be noted that the contour would intersect with the circular cut $\widehat{t_{1,j}t_{2,j}}$. The imaginary part of $X_j^+(\xi_j)$ on the left side of the cut is the same to that in Eq. (3.15). On the right side of the cut, the imaginary part of $X_j^-(\xi_j)$ can be expressed as

$$\arg X_j^-(\xi_j) = -\eta [\arg(\zeta_j - t_{1,j}) + 2k\pi] + (\eta - 1) \arg(\zeta_j - t_{2,j}) = \arg X_j^+(\xi_j) - 2k\pi\eta, \quad \xi_j \in \mathbf{c}_{0c,j} \quad (3.16b)$$

Combining the real part, Eq. (3.16b) would yield

$$X_j^+(\xi_j) - e^{i2k\pi\eta} \cdot X_j^-(\xi_j) = 0, \quad \xi_j \in \mathbf{c}_{0c,j} \quad (3.16b')$$

Eq. (3.16b') shares the same formation and definition domain as those in Eq. (3.13b), and $X_j(\xi_j)$ can be simulated as one of possible solution of $\varphi'_{0,j}(\zeta_j)$, as long as $e^{i2k\pi\eta} = -\kappa^{-1}$ is satisfied. The undetermined value of η can be correspondingly obtained as

$$\eta = \frac{1}{2k} + i \frac{\ln \kappa}{2k\pi} \quad (3.17)$$

where $\ln(-1) = i\pi$ for principal value of argument. For simplicity and consistency, we can take $k = 1$ in Eq. (3.17), and have

$$\eta = \frac{1}{2} + i \frac{\ln \kappa}{2\pi} \quad (3.17')$$

Substituting the determined value of η in Eq. (3.17') into Eq. (3.14) yields

$$X_j(\zeta_j) = (\zeta_j - t_{1,j})^{-\frac{1}{2}-i\lambda} (\zeta_j - t_{2,j})^{-\frac{1}{2}+i\lambda}, \quad \lambda = \frac{\ln \kappa}{2\pi}, \quad \zeta_j \in \overline{\omega}_j \cup \omega_j^- \setminus \{t_{1,j}, t_{2,j}\} \quad (3.14')$$

Eq. (3.14') is in the same formation of Eq. (3.14), and satisfies Eq. (3.13b), and therefore can be treated a simulation of the solution of Eq. (3.13).

However, our problem consists of not only the mixed boundaries along ground surface in Eq. (3.13), but also the traction boundary condition in Eq. (3.8). The left-hand side of Eq. (3.8) contains both complex potentials $\varphi'_{0,j}(\zeta_j)$ and $\psi'_{0,j}(\zeta_j)$ to be determined, which should be analytic within the mapping region $\overline{\omega}_j \setminus \{t_{1,j}, t_{2,j}\}$. To simulate the possible solution, we may assume the general solution of $\varphi'_{0,j}(\zeta_j)$ as a combination of $X_j(\zeta_j)$ and an arbitrary analytic function, which should be defined within the mapping region $\overline{\omega}_j \setminus \{t_{1,j}, t_{2,j}\}$ with two poles of origin and complex infinity. Therefore, the general solution of $\varphi'_{0,j}(\zeta_j)$ can be expressed as

$$\varphi'_{0,j}(\zeta_j) = X_j(\zeta_j) \sum_{n=-\infty}^{\infty} f_{j,n} \zeta_j^n, \quad \zeta_j \in \overline{\omega}_j \setminus \{t_{1,j}, t_{2,j}\} \quad (3.18)$$

where $f_{j,n}$ denote complex coefficients for j^{th} cavity to be determined. Comparing to Eq. (3.14'), the definition domain of item $X_j(\zeta)$ in Eq. (3.18) is reduced from $\overline{\omega}_j \cup \omega_j^- \setminus \{t_{1,j}, t_{2,j}\}$ to $\overline{\omega}_j \setminus \{t_{1,j}, t_{2,j}\}$. Whereas in theory, $X_j(\zeta_j)$ and the Laurent series behind in Eq. (3.18) are both capable being analytic in mapping region $\overline{\omega}_j \cup \omega_j^- \setminus \{t_{1,j}, t_{2,j}\}$. We should emphasize that Eq. (3.18) is only one of the possible solution formations to simulate the complex potential $\varphi'_{0,j}(\zeta_j)$.

The complex items with complex fractional power $X_j(\zeta_j)$ in Eq. (3.14) is difficult to reach computational results, and can be subsequently expanded into Taylor series near the poles origin and complex infinity due to its possible definition region $\bar{\omega}_j \cup \omega_j^- \setminus \{t_{1,j}, t_{2,j}\}$, respectively, as

$$X_j(\zeta_j) = \begin{cases} \sum_{k=0}^{\infty} \alpha_{j,k} \zeta_j^k, & \zeta_j \in \omega_j^+ \\ \sum_{k=0}^{\infty} \beta_{j,k} \zeta_j^{-k}, & \zeta_j \in \omega_j^- \end{cases} \quad (3.19)$$

where

$$\begin{cases} \alpha_{j,0} = -t_{1,j}^{-\frac{1}{2}-i\lambda} t_{2,j}^{-\frac{1}{2}+i\lambda} \\ \alpha_{j,k} = -t_{1,j}^{-\frac{1}{2}-i\lambda} t_{2,j}^{-\frac{1}{2}+i\lambda} \cdot (-1)^k \left(c_k t_{1,j}^{-k} + \bar{c}_k t_{2,j}^{-k} + \sum_{l=1}^{k-1} c_l \bar{c}_{k-l} \cdot t_{1,j}^{-l} t_{2,j}^{-k+l} \right), & k \geq 1 \end{cases} \quad (3.20a)$$

$$\begin{cases} \beta_{j,0} = 0 \\ \beta_{j,1} = 1 \\ \beta_{j,k} = (-1)^{k-1} \left(c_{k-1} t_{1,j}^{k-1} + \bar{c}_{k-1} t_{2,j}^{k-1} + \sum_{l=1}^{k-2} c_l \bar{c}_{k-1-l} \cdot t_{1,j}^l t_{2,j}^{k-1-l} \right), & k \geq 2 \end{cases} \quad (3.20b)$$

with

$$c_k = \prod_{l=1}^k \left(\frac{1}{2} - i\lambda - l \right) / k! \quad (3.20c)$$

We may note that the expansions in Eq. (3.19) are conducted in mapping regions ω_j^+ and ω_j^- , respectively, while the constrained segments $\mathbf{c}_{0c,j}$ and free segments $\mathbf{c}_{0f,j}$ along the exterior periphery of the mapping unit annuli, as well as the singularities $t_{1,j}$ and $t_{2,j}$, are not included.

It should be addressed that the definition domain of Eq. (3.19) is contained within that of Eq. (3.18). Before substituting Eq. (3.19) into Eq. (3.18) for computation convenience, we should artificially alter the definition domain $\bar{\omega}_j \setminus \{t_{1,j}, t_{2,j}\}$ of Eq. (3.18) into subdomains ω_j^+ and ω_j^- , according to Eq. (3.19). Then we can substituting Eq. (3.19) into Eq. (3.18) to obtain

$$\varphi'_{0,j}(\zeta_j) = \sum_{k=-\infty}^{\infty} A_{j,k} \zeta_j^k, \quad \zeta_j \in \omega_j^+ \quad (3.21a)$$

$$\varphi'_{0,j}(\zeta_j) = \sum_{k=-\infty}^{\infty} B_{j,k} \zeta_j^k, \quad \zeta_j \in \omega_j^- \quad (3.21b)$$

where

$$A_{j,k} = \sum_{n=-\infty}^k \alpha_{j,k-n} f_{j,n} \quad (3.22a)$$

$$B_{j,k} = \sum_{n=k}^{\infty} \beta_{j,-k+n} f_{j,n} \quad (3.22b)$$

Eq. (3.21) provides expanding expressions of complex potential $\varphi'_{0,j}(\zeta_j)$ with undetermined coefficients $f_{j,n}$ in Eq. (3.18), and alters the definition domain from $\overline{\omega}_j \setminus \{t_{1,j}, t_{2,j}\}$ to $\omega_j^+ \cup \omega_j^-$ temporarily for computation convenience.

Eqs. (3.21a) and (3.21b) are Taylor expansions of $X_j(\zeta_j)$ from ω_j^+ and ω_j^- sides, respectively, which are both analytic for unit arc segments $\mathbf{c}_{0c,j}$ and $\mathbf{c}_{0f,j}$. Subsequently, the constrained segments $\mathbf{c}_{0c,j}$ and free segments $\mathbf{c}_{0f,j}$ of exterior peripheries of the mapping unit annuli should be seen as boundary values when $\zeta_j \rightarrow \sigma_j$, and definition domain of Eq. (3.21) can be updated as

$$\varphi'_{0,j}(\zeta_j) = \sum_{k=-\infty}^{\infty} A_{j,k} \zeta_j^k, \quad \zeta_j \in \omega_j^+ \cup \mathbf{c}_{0c,j} \cup \mathbf{c}_{0f,j} \quad (3.21a')$$

$$\varphi'_{0,j}(\zeta_j) = \sum_{k=-\infty}^{\infty} B_{j,k} \zeta_j^k, \quad \zeta_j \in \omega_j^- \cup \mathbf{c}_{0c,j} \cup \mathbf{c}_{0f,j} \quad (3.21b')$$

We should note that the singularities $t_{1,j}$ and $t_{2,j}$ are not included in Eqs. (3.21a') and (3.21b'). Besides, $\omega_j^+ \cup \mathbf{c}_{0c,j} \cup \mathbf{c}_{0f,j} = \overline{\omega}_j \setminus \{t_{1,j}, t_{2,j}\}$. Respectively comparing to Eqs. (3.21a) and (3.21b), Eqs. (3.21a') and (3.21b') fill the missing definition domain $\mathbf{c}_{0f,j}$ and $\mathbf{c}_{0c,j}$. The union of the definition domains of Eqs. (3.21a') and (3.21b') would complete the original definition domain of $\varphi'_{0,j}(\zeta_j)$ in Eq. (3.18).

Now we may provide formation of the other complex potential $\psi'_{0,j}(\zeta_j)$ using Eqs. (3.21a') and (3.21b') below. Eq. (3.9) can be formulated as

$$\psi'_{0,j}(t_j) = \frac{\overline{t_j}}{t_j} \overline{\varphi'_{0,j}(t_j)} + \frac{\overline{t_j} \overline{z'_j(t_j)}}{t_j z'_j(t_j)} \varphi'_{0,j}(t_j) + \frac{\overline{z_j(t_j)} \overline{z''_j(t_j)}}{[z'_j(t_j)]^2} \varphi'_{0,j}(t_j) - \frac{\overline{z_j(t_j)}}{z'_j(t_j)} \varphi''_{0,j}(t_j), \quad t_j \in \mathbf{c}_{0f,j} \quad (3.23)$$

Eq. (3.23) can be rewritten into a more compact manner as

$$\psi'_{0,j}(t_j) = \frac{\overline{t_j}}{t_j} \overline{\varphi'_{0,j}(t_j)} - d \left[\frac{\overline{z_j(t_j)}}{z'_j(t_j)} \varphi'_{0,j}(t_j) \right] / dt_j, \quad t_j \in \mathbf{c}_{0f,j} \quad (3.23')$$

If we note that $\overline{z_j(t_j)} = z_j(t_j)$ denotes the x axis in the physical plane $z = x + iy$ and $\overline{t_j} = t_j^{-1}$ on the segment $\mathbf{c}_{0f,j}$ of the unit annuli $\overline{\omega}_j$, Eq. (3.23') can be transformed as

$$\psi'_{0,j}(t_j) = \frac{1}{t_j^2} \overline{\varphi'_{0,j}(t_j^{-1})} - d \left[\frac{z_j(t_j)}{z'_j(t_j)} \varphi'_{0,j}(t_j) \right] / dt_j, \quad t_j \in \mathbf{c}_{0f,j} \quad (3.24)$$

In above deductions, the closed-form expression of the other complex potential $\psi'_{0,j}(\zeta_j)$ is still not given, we may assume the following formation as

$$\psi'_{0,j}(\zeta_j) = \frac{1}{\zeta_j^2} \overline{\varphi'_{0,j}(\zeta_j^{-1})} - d \left[\frac{z_j(\zeta_j)}{z'_j(\zeta_j)} \varphi'_{0,j}(\zeta_j) \right] / d\zeta_j, \quad \zeta_j \in \overline{\omega}_j \setminus \{t_{1,j}, t_{2,j}\} \quad (3.25)$$

Apparently, when $\zeta_j \rightarrow t_j \in \mathbf{c}_{0f,j}$, Eq. (3.25) would turn into its boundary value in Eq. (3.23) inversely using $t_j^{-1} = \overline{t_j}$ in the first item and $z_j(t_j) = \overline{z_j(t_j)}$ in the second item, respectively. When

$\zeta_j \in \overline{\omega}_j \setminus \{t_{1,j}, t_{2,j}\}$, $\zeta_j^{-1} \in \omega_j^- \cup \mathbf{c}_{0c,j} \cup \mathbf{c}_{0f,j}$, and the first item of Eq. (3.25) can be expanded using Eq. (3.21b') as

$$\psi'_{0,j}(\zeta_j) = \sum_{k=-\infty}^{\infty} \overline{B}_{j,-k-2} \zeta_j^k - d \left[\frac{z_j(\zeta_j)}{z'_j(\zeta_j)} \varphi'_{0,j}(\zeta_j) \right] / d\zeta_j, \quad \zeta_j \in \overline{\omega}_j \setminus \{t_{1,j}, t_{2,j}\} \quad (3.25')$$

Eq. (3.25') provides expressions of complex potential $\psi'_{0,j}(\zeta_j)$ with undetermined coefficients $f_{j,n}$ in Eq. (3.18) in the same definition domain. In the following deductions, we should determine coefficients $f_{j,n}$ in Eq. (3.18) using the boundary condition along cavity boundary in Eq. (3.8).

Substituting Eqs. (3.3b), (3.21a'), and (3.25') (we may note that all three equations share the same definition domain $\overline{\omega}_j \setminus \{t_{1,j}, t_{2,j}\}$) into the left-hand side of Eq. (3.8) yields

$$\begin{aligned} & \sum_{\substack{k=-\infty \\ k \neq 0}}^{\infty} \left(A_{j,k-1} \frac{\alpha_j^k}{k} \sigma_j^k + B_{j,-k-1} \frac{\alpha_j^k}{k} \sigma_j^{-k} \right) + \frac{z_j(\alpha_j \sigma_j) - \overline{z_j(\alpha_j \sigma_j)}}{z'_j(\alpha_j \sigma_j)} \sum_{k=-\infty}^{\infty} \overline{A}_{j,k} \alpha_j^k \sigma_j^{-k} \\ & + (A_{j,-1} + B_{j,-1}) \ln \alpha_j + C_{a,j} + (A_{j,-1} - B_{j,-1}) \text{Ln} \sigma_j = -\gamma \int_{\mathbf{c}_j} y(s_j) \left[k_x \frac{\text{id}y(s_j)}{d\sigma_j} + \frac{dx(s_j)}{d\sigma_j} \right] d\sigma_j \end{aligned} \quad (3.26)$$

where $C_{a,j}$ denotes an arbitrary complex integral constant, Ln denotes the possibly multi-valued natural logarithm. The mapping item and the integrand of the right-hand side of Eq. (3.26) can be expanded using the sample point method [34, 35] as

$$\frac{z_j(\alpha_j \sigma_j) - \overline{z_j(\alpha_j \sigma_j)}}{z'_j(\alpha_j \sigma_j)} = \sum_{k=-\infty}^{\infty} d_{j,k} \sigma_j^k \quad (3.27a)$$

$$y(s_j) \left[k_x \frac{\text{id}y(s_j)}{d\sigma_j} + \frac{dx(s_j)}{d\sigma_j} \right] = \sum_{k=-\infty}^{\infty} h_{j,k} \sigma_j^k \quad (3.27b)$$

Then the right-hand side of Eq. (3.26) can be integrated using Eq. (3.27b) as

$$-\gamma \int_{\mathbf{c}_j} \left[k_x \frac{\text{id}y(s_j)}{d\sigma_j} + \frac{dx(s_j)}{d\sigma_j} \right] d\sigma_j = \sum_{\substack{k=-\infty \\ k \neq 0}}^{\infty} I_{j,k} \sigma_j^k + I_{j,0} \text{Ln} \sigma_j \quad (3.28)$$

where

$$\begin{cases} I_{j,k} = -\gamma \frac{h_{j,k-1}}{k}, & k \neq 0 \\ I_{j,0} = -\gamma h_{j,-1} \end{cases} \quad (3.29)$$

Substituting Eqs. (3.21), (3.27a), and (3.28) into Eq. (3.26) and comparing the coefficients of same power of σ_j yields

$$A_{j,-k-1} = -k \alpha_j^k I_{j,-k} + \alpha_j^{2k} B_{j,-k-1} + k \alpha_j^{2k} \sum_{l=-\infty}^{\infty} \alpha_j^l d_{j,k} \overline{A}_{j,l+k}, \quad k \geq 1 \quad (3.30a)$$

$$B_{j,k-1} = -k \alpha_j^k I_{j,k} + \alpha_j^{2k} A_{j,k-1} + k \sum_{l=-\infty}^{\infty} \alpha_j^l d_{j,k} \overline{A}_{j,l-k}, \quad k \geq 1 \quad (3.30b)$$

$$A_{j,-1} - B_{j,-1} = I_{j,0} \quad (3.31)$$

The resultant equilibrium in Eq. (2.17) can be transformed using residual theorem as [32, 33, 34, 35]

$$A_{j,-1} - B_{j,-1} = -i \frac{R_y^{0,j}}{2\pi} \quad (3.31')$$

Eqs. (3.31) and (3.31') reveal an implicit equilibrium as

$$I_{j,0} = -\frac{i\gamma}{2\pi} \iint_{D_j} dx dy \quad (3.32)$$

Eq. (3.32) should always be numerically examined. Furthermore, Eqs. (3.30) and (3.31) derived from Eqs. (3.13) and (3.8) only determines the first derivatives $\varphi'_{0,j}(\zeta_j)$ and $\psi'_{0,j}(\zeta_j)$ to be analytic and single-valued, however, the displacement in Eq. (3.3c), which contains the original functions $\varphi_{0,j}(\zeta_j)$ and $\psi_{0,j}(\zeta_j)$, should be also analytic and single-valued. To guarantee the single-valuedness of displacement in Eq. (3.3c), the follow equilibrium should be established as [32, 33, 34, 35]

$$\kappa A_{j,-1} + B_{j,-1} = 0 \quad (3.33)$$

Eqs. (3.31) and (3.33) give the following invariants unaffected by conformal mappings as

$$A_{j,-1} = \frac{I_{j,0}}{1 + \kappa} \quad (3.34a)$$

$$B_{j,-1} = \frac{-\kappa I_{j,0}}{1 + \kappa} \quad (3.34b)$$

Substituting Eq. (3.22) into the left-hand sides of Eqs. (3.30) and (3.34) gives well-defined simultaneous complex linear system on f_n ($-\infty < n < \infty$) as

$$\begin{cases} \sum_{n=1}^{\infty} \alpha_{j,-1+n} f_{j,n} = \frac{I_{j,0}}{1 + \kappa} \\ \sum_{n=k+1}^{\infty} \alpha_{j,-k-1+n} f_{j,-n} = -k\alpha_j^k I_{j,-k} + \alpha_j^{2k} B_{j,-k-1} + k\alpha_j^k \sum_{l=-\infty}^{\infty} \alpha_j^l d_{j,k} \bar{A}_{j,l+k}, \quad k \geq 1 \end{cases} \quad (3.35a)$$

$$\begin{cases} \sum_{n=0}^{\infty} \beta_{j,1+n} f_{j,n} = \frac{-\kappa I_{j,0}}{1 + \kappa} \\ \sum_{n=k}^{\infty} \beta_{j,-k+1+n} f_{j,n} = -k\alpha_j^k I_{j,k} + \alpha_j^{2k} A_{j,k-1} + k \sum_{l=-\infty}^{\infty} \alpha_j^l d_{j,k} \bar{A}_{j,l-k}, \quad k \geq 1 \end{cases} \quad (3.35b)$$

Eq. (3.35) can be solved in the iterative method in Refs [32, 33, 34, 35] to uniquely determine f_n in Eq. (3.18), so that the complex potentials in Eqs. (3.21a') and (3.25) can be subsequently determined for further solution of stress and displacement of sequential shallow tunnelling.

3.3. Stress and displacement fields of sequential shallow tunnelling

Replacing $s_j = \alpha_j \sigma_j$ with $\zeta_j = \rho_j \sigma_j$ in Eqs. (3.8) and (3.26) yields the integration of the curvilinear traction components mapped onto the mapping annuli $\bar{\omega}_j \setminus \{t_{1,j}, t_{2,j}\}$ for a given polar radius ρ_j as

$$\begin{aligned} & \int z'_j(\rho_j \sigma_j) \left[\sigma_\rho^{0,j}(\rho_j \sigma_j) + i\tau_{\rho\theta}^{0,j}(\rho_j \sigma_j) \right] d(\rho_j \sigma_j) \\ &= \sum_{\substack{k=-\infty \\ k \neq 0}}^{\infty} \left(A_{j,k-1} \frac{\rho_j^k}{k} - B_{j,k-1} \frac{\rho_j^{-k}}{k} \right) \sigma_j^k + \sum_{k=-\infty}^{\infty} \sum_{l=-\infty}^{\infty} g_{j,l}(\rho_j) \bar{A}_{j,l-k} \rho_j^{l-k} \sigma_j^k \\ &+ (A_{j,-1} + B_{j,-1}) \ln \rho_j + (A_{j,-1} - B_{j,-1}) \text{Ln} \sigma_j + C_{a,j}, \quad \alpha_j \leq \rho_j \leq 1, \sigma_j \neq t_{1,j}, t_{2,j} \end{aligned} \quad (3.36)$$

where

$$\sum_{k=-\infty}^{\infty} g_{j,k}(\rho_j) \sigma_j^k = \frac{z_j(\rho_j \sigma_j) - \overline{z_j(\rho_j \sigma_j)}}{z'_j(\rho_j \sigma_j)} \quad (3.37)$$

When $\rho_j \rightarrow \alpha_j$, Eq. (3.37) would be degenerated into Eq. (3.27). When $\rho_j \rightarrow 1$, the right-hand side of Eq. (3.37) would be zero, since $\overline{z_j(\sigma_j)} = z_j(\sigma_j)$ denotes the x axis in the physical plane $z = x + iy$.

The derivation of Eq. (3.36) gives the expansion of Eq. (3.3b) as

$$\sigma_\rho^{0,j}(\rho_j \sigma_j) + i\tau_{\rho\theta}^{0,j}(\rho_j \sigma_j) = \frac{1}{z'_j(\rho_j \sigma_j)} \sum_{k=-\infty}^{\infty} \left(\begin{aligned} & A_{j,k} \rho_j^k - B_{j,k} \rho_j^{-k-2} \\ & + (k+1) \sum_{l=-\infty}^{\infty} g_{j,l}(\rho_j) \bar{A}_{j,l-k-1} \rho_j^{l-k-2} \end{aligned} \right) \sigma_j^k, \quad \begin{aligned} & \alpha_j \leq \rho_j \leq 1 \\ & \sigma_j \neq t_{1,j}, t_{2,j} \end{aligned} \quad (3.38a)$$

Eqs. (3.3a) and (3.3c) can be respectively expanded as

$$\sigma_\theta^{0,j}(\rho_j \sigma_j) + \sigma_\rho^{0,j}(\rho_j \sigma_j) = 4\Re \left[\frac{1}{z'_j(\rho_j \sigma_j)} \sum_{k=-\infty}^{\infty} A_{j,k} \rho_j^k \sigma_j^k \right], \quad \begin{aligned} & \alpha_j \leq \rho_j \leq 1 \\ & \sigma_j \neq t_{1,j}, t_{2,j} \end{aligned} \quad (3.38b)$$

$$\begin{aligned} 2G[u_{0,j}(\rho_j \sigma_j) + iv_{0,j}(\rho_j \sigma_j)] &= \sum_{\substack{k=-\infty \\ k \neq 0}}^{\infty} \frac{1}{k} (\kappa A_{j,k-1} \rho_j^k \sigma_j^k + B_{j,k-1} \rho_j^{-k} \sigma_j^k) + C_0 + (\kappa A_{j,-1} - B_{j,-1}) \ln \rho_j \\ &- \sum_{k=-\infty}^{\infty} \sum_{l=-\infty}^{\infty} g_{j,l}(\rho_j) \bar{A}_{j,l-k} \rho_j^{l-k} \sigma_j^k, \quad \alpha_j \leq \rho_j \leq 1, \sigma_j \neq t_{1,j}, t_{2,j} \end{aligned} \quad (3.38c)$$

with

$$C_0 = - \sum_{\substack{k=-\infty \\ k \neq 0}}^{k=\infty} \frac{1}{k} (\kappa A_{j,k-1} + B_{j,k-1})$$

The initial stress field in Eq. (2.2) can be mapped onto the mapping annuli $\bar{\omega}_j$ as

$$\begin{cases} \sigma_\theta^0(\rho_j \sigma_j) + \sigma_\rho^0(\rho_j \sigma_j) = \sigma_y^0[z_j(\rho_j \sigma_j)] + \sigma_x^0[z_j(\rho_j \sigma_j)] \\ \sigma_\theta^0(\rho_j \sigma_j) - \sigma_\rho^0(\rho_j \sigma_j) + 2i\tau_{\rho\theta}^0(\rho_j \sigma_j) = \{ \sigma_y^0[z_j(\rho_j \sigma_j)] - \sigma_x^0[z_j(\rho_j \sigma_j)] + 2i\tau_{xy}[z(\rho_j \sigma_j)] \} \cdot \frac{z'_j(\rho_j \sigma_j)}{z'_j(\rho_j \sigma_j)} \cdot \sigma_j^2, \end{cases} \quad \begin{aligned} & \alpha_j \leq \rho_j \\ & \sigma_j \neq t_{1,j} \end{aligned} \quad (2.2')$$

where σ_θ^0 , σ_ρ^0 , and $\tau_{\rho\theta}^0$ denote hoop, radial, and shear components of the initial stress field mapped onto the mapping unit annuli $\bar{\omega}_j$, respectively.

According to Eqs. (3.38) and (2.2'), the total curvilinear stress field mapped onto mapping unit annuli $\bar{\omega}_j$ can be obtained as

$$\begin{cases} \sigma_\theta^j(\rho_j\sigma_j) = \sigma_\theta^0(\rho_j\sigma_j) + \sigma_\theta^{0,j}(\rho_j\sigma_j) \\ \sigma_\rho^j(\rho_j\sigma_j) = \sigma_\rho^0(\rho_j\sigma_j) + \sigma_\rho^{0,j}(\rho_j\sigma_j) \\ \tau_{\rho\theta}^j(\rho_j\sigma_j) = \tau_{\rho\theta}^0(\rho_j\sigma_j) + \tau_{\rho\theta}^{0,j}(\rho_j\sigma_j) \end{cases}, \quad \begin{matrix} \alpha_j \leq \rho_j \leq 1 \\ \sigma_j \neq t_{1,j}, t_{2,j} \end{matrix} \quad (3.39a)$$

where σ_θ^j , σ_ρ^j , and $\tau_{\rho\theta}^j$ denote hoop, radial, and tangential components of total curvilinear stress mapped onto the mapping unit annuli $\bar{\omega}_j$ along the circles of radii $|\zeta_j| = \rho_j$, respectively. The displacement field mapped onto mapping unit annuli $\bar{\omega}_j$ can be obtained as

$$u_j(\rho_j\sigma_j) + iv_j(\rho_j\sigma_j) = u_j[z_j(\rho_j\sigma_j)] + iv_j[z_j(\rho_j\sigma_j)], \quad \alpha_j \leq \rho_j \leq 1, \sigma_j \neq t_{1,j}, t_{2,j} \quad (3.39b)$$

Significantly, when $\rho_j \rightarrow \alpha_j$, Eq. (3.39a) gives the Mises stress (numerically equal to the absolute value of $\sigma_\theta^j(\alpha_j\sigma_j)$) and the residual stresses (radial component $\sigma_\rho^j(\alpha_j\sigma_j)$ and tangential component $\tau_{\rho\theta}^j(\alpha_j\sigma_j)$) along cavity boundary \mathbf{C}_j caused by j^{th} stage excavation; Eq. (3.39b) gives the horizontal and vertical deformation along cavity boundary \mathbf{C}_j .

The curvilinear stress and displacement fields in Eq. (3.39) can be mapped onto rectangular ones as

$$\begin{cases} \sigma_y^j[z_j(\zeta_j)] + \sigma_x^j[z_j(\zeta_j)] = \sigma_\theta^j(\zeta_j) + \sigma_\rho^j(\zeta_j) \\ \sigma_y^j[z_j(\zeta_j)] - \sigma_x^j[z_j(\zeta_j)] + 2i\tau_{xy}^j[z_j(\zeta_j)] = \left[\sigma_\theta^j(\zeta_j) - \sigma_\rho^j(\zeta_j) + 2i\tau_{\rho\theta}^j(\zeta_j) \right] \cdot \frac{\bar{\zeta}_j}{\zeta_j} \cdot \frac{\overline{z_j'(\zeta_j)}}{z_j'(\zeta_j)}, \quad \zeta_j = \rho_j \cdot \sigma_j \end{cases} \quad (3.40a)$$

$$u_j[z_j(\zeta_j)] + iv_j[z_j(\zeta_j)] = u_j(\zeta_j) + v_j(\zeta_j), \quad \zeta_j = \rho_j \cdot \sigma_j \quad (3.40b)$$

where σ_x^j , σ_y^j , and τ_{xy}^j denote horizontal, vertical, and shear components of the total stress field after j^{th} -stage excavation, respectively.

4. Numerical case and verification

The solution in Section 3 is analytical with infinite Laurent series of $f_{j,n}$ in Eq. (3.18), which should be bilaterally truncated into $2M_j + 1$ items to reach numerical results. The coefficient series in Eq. (3.22) should be truncated as

$$A_{j,k} = \sum_{n=-M_j}^k \alpha_{j,k+n} f_{j,-n} \quad (3.22a')$$

$$B_{j,k} = \sum_{n=k}^{M_j} \beta_{j,-k+n} f_{j,n} \quad (3.22b')$$

where $j = 1, 2, 3, \dots, N$. The infinite series to obtain solution of $f_{j,n}$ in Eqs. (3.35) should be truncated as well. Correspondingly, the stress and displacement fields in Section 3.3 should be truncated, which leads to numerical errors in oscillation form of Gibbs phenomena [32, 34]. To

reduce the Gibbs phenomena, the Lanczos filtering is applied in Eq. (3.38) to replace $A_{j,k}$ and $B_{j,k}$ with $A_{j,k} \cdot L_k$ and $B_{j,k} \cdot L_k$, respectively, where

$$L_k = \begin{cases} 1, & k = 0 \\ \sin\left(\frac{k}{M_j}\pi\right) / \left(\frac{k}{M_j}\pi\right), & \text{otherwise} \end{cases} \quad (4.1)$$

with $-M_j \leq k \leq M_j$.

In this section, a numerical case of 4 stage shallow tunnelling is performed to validate the present analytical solution by comparing with a corresponding finite element solution. The present analytical solution is conducted using the programming language FORTRAN of compiler GCC (version 14.1.1). The linear systems are solved using the DGESV and ZGESV packages of LAPACK (version 3.12.0). The figures are plotted using GNU PLOT (version 6.0). All analytical codes and finite element model are released in author Luobin Lin's github repository: github.com/luobinlin987/sequential-shallow-tunnelling.

4.1. Cavity geometries and bidirectional conformal mappings of sequential shallow tunnelling

The numerical case of sequential shallow tunnelling takes the geometry of the 4-stage excavation in Fig. 2b, while the sharp corner smoothing technique is applied to adapt the numerical schemes of bidirectional conformal mapping in Appendix A.2. Thus, the cavity boundaries of 4-stage excavation can be analytically expressed as

$$\text{Stage 1 : } \begin{cases} x^2 + (y + 10)^2 = 5^2, & -5 \leq x \leq 0, -10 \leq y \leq -5 \\ (x + 4.5)^2 + (y + 10)^2 = 0.5^2, & -5 \leq x \leq -4.5, -10.5 \leq y \leq -10 \\ y = -10.5, & -4.5 \leq x \leq 0 \\ x^2 + (y + 10)^2 = 0.5^2, & 0 \leq x \leq 0.5, -10.5 \leq y \leq -10 \\ x = 0.5, & -10 \leq y \leq -5.5 \\ x^2 + (y + 5.5)^2 = 0.5^2, & 0 \leq x \leq 0.5, -5.5 \leq y \leq -5 \end{cases} \quad (4.2a)$$

$$\text{Stage 2 : } \begin{cases} x^2 + (y + 10)^2 = 5^2, & -5 \leq x \leq 5, -10 \leq y \leq -5 \\ (x + 4.5)^2 + (y + 10)^2 = 0.5^2, & -5 \leq x \leq -4.5, -10.5 \leq y \leq -10 \\ y = -10.5, & -4.5 \leq x \leq 4.5 \\ (x - 4.5)^2 + (y + 10)^2 = 0.5^2, & 4.5 \leq x \leq 5, -10.5 \leq y \leq -10 \end{cases} \quad (4.2b)$$

$$\text{Stage 3 : } \begin{cases} x^2 + (y + 10)^2 = 5^2, & -5 \leq x \leq 5, -10 \leq y \leq -5 \\ x = -5, & -14.5 \leq y \leq -10 \\ (x + 4.5)^2 + (y + 14.5)^2 = 0.5^2, & -5 \leq x \leq -4.5, -15 \leq y \leq -14.5 \\ y = -15, & -4.5 \leq x \leq 0 \\ x^2 + (y + 14.5)^2 = 0.5^2, & 0 \leq x \leq 0.5, -15 \leq y \leq -14.5 \\ x = 0.5, & -14.5 \leq y \leq -11 \\ (x - 1)^2 + (y + 11)^2 = 0.5^2, & 0.5 \leq x \leq 1, -11 \leq y \leq -10.5 \\ y = -10.5, & 1 \leq x \leq 4.5 \\ (x - 4.5)^2 + (y + 10)^2 = 0.5^2, & 4.5 \leq x \leq 5, -10.5 \leq y \leq -10 \end{cases} \quad (4.2c)$$

$$\text{Stage 4 : } \begin{cases} x^2 + (y + 10)^2 = 5^2, & -5 \leq x \leq 5, -10 \leq y \leq -5 \\ x = -5, & -14.5 \leq y \leq -10 \\ (x + 4.5)^2 + (y + 14.5)^2 = 0.5^2, & -5 \leq x \leq -4.5, -15 \leq y \leq -14.5 \\ y = -15, & -4.5 \leq x \leq 4.5 \\ (x - 4.5)^2 + (y + 14.5)^2 = 0.5^2, & 4.5 \leq x \leq 5, -15 \leq y \leq -14.5 \\ x = 5, & -14.5 \leq y \leq -10 \end{cases} \quad (4.2d)$$

With the geometrical expressions in Eq. (4.2), the bidirectional conformal mappings of the 4-stage sequential shallow tunnelling can be obtained in Fig. 5, in which the collocation points are taken in the following pattern for good accuracy after trial computations: (1) 30 points are uniformly selected along the 90° arc of 0.5m radius; (2) 90 points are uniformly selected along the 90° arc of 5m radius; 60 points are uniformly selected along the rest straight lines. The collocation points along the cavity boundary in the physical plane z are denoted by $z_{j,i}^f$, where j denotes the excavation stage, i denotes the collocation point number, f denotes the word "forward". After trial computations, the assignment factors take $K_j^0 = k_j^0 = 2.2$ and $K_j^1 = k_j^1 = 1.5$, while $w_j^c = -2.5 - 7.5i$ and $w_{j,0} = 0.9\beta$, where $\beta = 5$ and $j = 1, 2, 3, 4$.

To quantitatively determine the accuracy of the bidirectional conformal mapping, the following criteria are established as

$$\varepsilon_j = \max |z_{j,i}^{m,b} - z_{j,i}^{m,f}|, \quad i = 1, 2, 3, \dots, N_j \quad (4.3)$$

where $z_{j,i}^{m,f}$ denote the midpoints of the selected collocation points $z_{j,i}^f$, and can be computed as

$$z_{j,i}^{m,f} = \frac{1}{2}(z_{j,i}^f + z_{j,i+1}^f), \quad i = 1, 2, 3, \dots, N_j$$

$z_{j,i}^{m,b}$ denote the coordinates of the corresponding midpoints $z_{j,i}^{m,f}$ after forward and backward conformal mappings, which can be computed in the following procedure.

Via Eq. (A.1a), the midpoints of the collocation points $z_{j,i}^{m,f}$ can be forwardly mapped onto corresponding mapping points $w_{j,i}^{m,f}$ in the interval mapping plane Ω_j^w . Then via Eq. (A.2a'), the midpoints in the mapping plane ω_j can be computed as $\zeta_{j,i}^{m,f}$. Subsequently, the midpoints for backward conformal mapping in the mapping plane ω_j are given by only preserving the polar angles as

$$\zeta_{j,i}^{m,b} = \alpha_j \cdot \exp(i \arg \zeta_{j,i}^{m,f}) \quad (4.4)$$

where b in the superscript denotes "backward". Apparently, slight differences between $\zeta_{j,i}^{m,b}$ and $\zeta_{j,i}^{m,f}$ should exist. Whereafter, the backward midpoints in the interval mapping plane Ω_j^w can be computed as $w_{j,i}^{m,b}$ via Eq. (A.6). Finally, the backward midpoints $z_{j,i}^{m,b}$ in the physical plane Ω_j can be computed via Eq. (A.1b). Therefore, ε_j in Eq. (4.3) should be able to present the maximum difference between the original midpoints and computed ones along cavity boundary for sequential excavation stages.

The orthogonal grids and corresponding values of ε_j in Fig. 5 show that the bidirectional conformal mapping in Appendix A is very adaptive, and can be used to conformally map a lower half plane containing an asymmetrical cavity of very complicated shape (see Fig. 5c). Therefore, the conformal mapping can be used in further mechanical computation. However, we should also note in Fig. 5c that the orthogonal grid near concave boundary would be thin (as marked), indicating that the accuracy for a lower half plane containing a concave cavity would be slightly compromised.

4.2. Comparisons with finite element solution

To validate the present analytical solution in Section 3, a finite element solution using software ABAQUS 2020 is performed for comparisons. The mechanical parameters of geomaterial are listed in Table 1, where the coordinates of the joint points T_1 and T_2 are deliberately located near the shallow tunnel for better illustration of boundary conditions along ground surface (see Figs. 9 and 10).

Table 1: Mechanical parameters of numerical case

$\gamma(\text{kN/m}^3)$	k_x	$E(\text{MPa})$	ν	x_0 (m)	M_j
20	0.8	20	0.3	10	250

The kN – m mechanical model of the finite element solution is shown in Fig. 6a, where the same 4-stage sequential shallow tunnelling is conducted. In Fig. 6a, the model geometry, geomaterial sketching, and seed distribution scheme outside of cavity are illustrated. In Fig. 6b, the 4-stage excavation procedure is marked by different colors, and more detailed seed distribution scheme of cavity boundaries is elaborated below: (1) 90 seeds are uniformly distributed along the 90° arcs of 5m; (2) 30 seeds are uniformly distributed along the 90° arcs of 0.5m; (3) 80 seeds are uniformly distributed along the rest straight lines. The meshing near cavity is shown in Fig. 6c, where the 4-stage excavation regions are marked with the same colors with the diagram of Fig. 6b. Both analytical and finite element solutions are in plane strain condition, thus, the 102499 finite elements use CPR4R type. The steps of finite element solution are listed in Table 2, where the 4 excavation stages are sequentially conducted, according to Fig. 6b.

Table 2: Steps of finite element solution

Step	Initial	Step 0	Step 1	Step 2	Step 3	Step 4
Procedure	(Initial)	Geostatic	Static,General	Static,General	Static,General	Static,General
Load	Applying constraints and geostress	Applying gravity	-	-	-	-
Interaction	-	-	Deactivating region I	Deactivating region II	Deactivating region III	Deactivating region IV

Substituting the mechanical parameters in Table 1 into the present solution and the finite element solution gives the results in Figs. 7-10. Fig. 7 shows the radial and tangential components of the residual stress along cavity boundaries of all four excavation stages, which are reduced by 10^{-2} for better illustration. In theory, the residual stress should be zero to accurately meet the zero boundary condition along cavity boundary (see Fig. 4). Fig. 7 indicates that both the present solution and the finite element solution agree to each other well for cavity boundaries with large curvature radii (a straight line has an infinite curvature radius). As for the rounded corners of small curvature radii, the present solution clearly surpasses the finite element solution. However, the residual stresses of 3rd stage excavation computed by the present solution contain significant errors near the concave boundary, indicating the defect of the present solution on concave cavity. Such a defect is caused by the bidirectional conformal mapping, and the curvilinear grid in Fig. 5c might provide certain clues. In Fig. 5c, the curvilinear grid density near the concave boundary is sparse and thin, which possibly causes loss of nearby mathematical information on the mechanical solution based on the curvilinear grid. Therefore, the present solution is more accurate than the finite element method for convex cavities.

Fig. 8 shows the Mises stress (reduced by 10^{-3}) and deformation (magnified by 10^2) along cavity boundaries for four excavation stages, and good agreements between these two solution are

observed, except that the Mises stresses near the rounded corners obtained by the present solution are acuter and larger than those obtained by the finite element solution. The results of the present solution should be more accurate than the finite element solution, since the residual stresses near the rounded corners obtained by the finite element in Fig. 7 contains much larger errors.

Fig. 9 shows the comparisons of vertical and shear stress components along ground surface between the present solution and the finite element solution in all four excavation stages, and good agreements are observed. To be specific, the zero tractions in the range $x \in [-10, 10]$ meet the requirement of the boundary condition in Eq. (2.18b), further indicating the correctness of the present solution.

Fig. 10 shows the comparisons of horizontal stress and ground deformation between the present solution and the finite element solution. The zero deformation in the range $x \in (\infty, -10] \cup [10, \infty)$ meets the requirement of the boundary condition in Eq. (2.18a), indicating that the present solution is capable of obtaining fixed far-field displacement as desired. The horizontal stress in the range $x \in (\infty, -10] \cup [10, \infty)$ between the present solution and the finite element solution is in good agreements. However, the horizontal stress and ground deformation in the range $x \in [-10, 10]$ between present solution and finite element solution show clear discrepancy, especially for 1st, 2nd, and 3rd excavation stages. Noting that the overall indices $\varepsilon_j (j = 1, 2, 3, 4)$ are small with order of magnitude 10^{-4} in Fig. 5, the bidirectional conformal mapping should be accurate, and such stress and ground deformation discrepancies are not caused by the mapping. The residual radial and tangential stress components in Fig. 7 (except for 7c), the vertical and shear stress components in the range $[-10, 10]$ in Fig. 9, and the ground deformation in the range $(-\infty, -10] \cup [10, \infty)$ in Fig. 10 match the corresponding mixed boundary conditions in Eqs. (2.15), (2.18b), and (2.18a), respectively. By contrast, the residual radial and tangential stress components of the finite element solution in Fig. 7 contain significant errors, especially around the rounded corners. Therefore, it would be reasonable to presume that the results computed by the present solution should be more accurate than those computed by the finite element method. In other words, the present solution should be more accurate than the finite element solution. However, we should also notice that the obvious errors of residual radial and tangential stress components computed by the present solution in Fig. 7c, which are probably caused by the thin orthogonal grid near the concave. Such errors indicate that the present solution may be inaccurate for excavation with concave cavity.

In summary, Figs. 7-10 show the validation of the boundary conditions of the present solution, and the good agreements between the present solution and corresponding finite element solution. Additionally, detailed discussions reveal that the present solution should be more accurate than the finite element solution. The present solution can be used for further application.

5. Parametric investigation

In this section, several practical applications of present solution are illustrated to show its possible usage in sequential shallow tunnelling. To be consistent and simple, the benchmark geometry and sequential excavation stages take the same ones in Section 4 (see Figs. 5 and 6b), and the benchmark parameters take the ones in Table 1.

5.1. Deformation along cavity boundary and solution convergence

Deformation along cavity boundary is significant in shallow tunnelling to estimate possible displacement around tunnel for further design optimization. In the validation of present solution in Section 4.2, the free ground surface is kept within the range of $x \in [-x_0, x_0]$ of $x_0 = 10\text{m}$ for good visualization and comparisons with finite element solution. However, the free ground

surface should range wider in practical shallow tunnelling, thus, we select the joint coordinate as $x_0 = 10^1, 10^2, 10^3, 10^4\text{m}$ to investigate the possible deformation along cavity boundary, while the rest parameters remain the same to the ones in Table 1.

The results of deformation along cavity boundary against joint point coordinate x_0 for four excavation stages are shown in Fig. 11 with a magnification of 10^2 times for better illustration. Fig. 11 shows overall upheavals of geomaterial around tunnels and clear inward contractions against cavity boundaries for all four excavation stages, which are coincident to engineering expectations. Moreover, the deformed cavity boundaries of $x_0 = 10^3\text{m}$ and $x_0 = 10^4\text{m}$ overlap to each other, which indicates the same deformation for large free ground segment C_{0f} above tunnel, as well as convergence of present solution.

5.2. Mises stress along cavity boundary

Mises stress along cavity boundary can be mechanically interpreted as the hoop stress along cavity boundary, which is significant in shallow tunnelling to estimate possible damage zones around cavity for consideration of necessary reinforcement measures. In the validation, the lateral coefficient is set to be $k_x = 0.8$, however, the shallow strata to excavate are complicated with different lateral coefficients. Thus, we select lateral coefficient as $k_x = 0.6, 0.8, 1.0, 1.2, 1.4, 1.6$ to investigate the variation of Mises stress along cavity boundaries of sequential shallow tunnelling, and the rest parameters remain the same to the ones in Table 1.

The results of Mises stress along cavity boundaries against lateral coefficient k_x for excavation stages are shown in Fig. 12 with reduction of 10^{-3} times for better illustration. Fig. 12 shows that a larger lateral coefficient would cause higher stress concentrations near the rounded corners during sequential excavation, since the overall stress of the initial stress field increases. Therefore, tunnel corners may need more reinforcement measures in sequential excavation to avoid possible damage of geomaterial due to stress concentration. Moreover, Fig. 12c shows that the Mises stress near the right bottom geomaterial is very approximate to zero, indicating possible negative hoop stress. In other words, possible tensile stress may exist near the to-be-excavated region of 3rd-stage excavation, which may be hazardous in construction safety, and necessary monitoring of nearby geomaterial should be conducted.

5.3. Stress concentration of rounded corners

Fig. 12 shows remarkable stress concentrations near the corners during sequential shallow tunnelling, thus, the reduction of stress concentration near corners should be discussed due to its high value in shallow tunnelling safety. Among the four excavation stages in Fig. 12, the geometry of the 3th excavation stage is the most complicated, and worthy of discussion. The corners are the geometrical cause of stress concentration in Fig. 12, thus, we select different radii of the rounded corners (see the excavation scheme in Fig. 6b) as 0.3, 0.4, 0.5, 0.6, 0.7, 0.8m, and the rest cavity geometry is the same to that in Fig. 5c. The mechanical parameters take the same values in Table 1.

The Mises stresses along cavity boundary of different radii of rounded corners for the 3rd-stage excavation are shown in Fig. 13 with reduction of 10^{-3} times for better illustration. Fig. 13 shows that as the radius of rounded corners increases from 0.3m to 0.8m, the stress concentration decreases from 1960.11kPa to 1247.92kPa by a remarkable 36.33%. Therefore, relatively large radius of rounded corners might be considered during sequential excavation to avoid overlarge stress concentration.

5.4. Sequential deformation along ground surface

Ground deformation due to sequential shallow tunnelling would probably affect nearby structures, and should be considered in tunnelling design. The previous validation and discussion show that present solution is capable of dealing with sequential excavation, thus, the deformation along ground surface due to sequential shallow tunnelling can be discussed. The parameters and geometry are the same to those in Section 5.2. Substituting all necessary parameters and geometry into the present solution gives the deformation along ground surface for four excavation stages of different lateral coefficients k_x in Fig. 14.

Fig. 14 shows two obvious patterns of deformation along ground surface related to excavation stages and lateral coefficient. The first obvious pattern is that the settlement trough along ground surface gradually turn to upheaval when the lateral coefficient k_x increases from 0.6 to 1.6, indicating that the ground is gradually squeezed for a larger lateral coefficient. The other obvious yet a bit of contradictory pattern is the sharp change of settlement trough of 2nd stage to upheaval of 3rd stage. The possible reason is the excavation regions in 3rd and 4th stages are deep enough to cause upheaval along ground surface.

6. Further discussions

In existing complex variable solutions of shallow tunnelling in gravitational geomaterial, the cavity shapes are always fully circular [24, 25] or symmetrically noncircular [26, 31, 30], and no sequential shallow tunnelling is considered. The most fundamental reason is the mathematical difficulty to seek a suitable conformal mapping scheme that could bidirectionally map a lower half plane containing a noncircular and possibly asymmetrical cavity with shape changing due to sequential excavation. The conformal mapping scheme in Appendix A extends the bidirectional stepwise conformal mapping in our previous study [35], which incorporates Charge Simulation Method [37] and Complex Dipole Simulation Method [38], to a lower half plane containing more complicated cavity shapes, as shown in Fig. 5 (especially in Fig. 5c). Furthermore, the validation in Figs. 7-10 indicate the possibilities to extend the mathematical usage of the complex variable method from the full shallow tunnelling schemes with circular or symmetrically noncircular cavity shapes in the existing complex variable solutions [24, 25, 26, 31, 30] to sequential ones with complicated interval cavity shapes (see Figs. 7c and 8c).

Despite the theoretical improvements mentioned above, several defects of the present solution exist, and should be disclosed as:

(1) The most obvious defect of the present solution is that the present solution requires the rest geomaterial after sequential excavation to always remain doubly-connected to hold topological consistence of geomaterial and ensure solvability of the solution, while temporary supports are not considered for seeking mechanical variation within gravitational geomaterial alone. Temporary supports are important mechanical structure in sequential shallow tunnelling, and would alter the stress and displacement fields within rest geomaterial. Ignoring temporary supports would compromise the present solution to a certain extent. In our future studies, the complex variable method should be further improved and modified to be able to consider liners and temporary supports.

(1') On the other hand, however, the numerical cases in Sections 4 and 5, which simulate the multi-stepwise upper half vertical subdivision method in Fig. 2c without consideration of temporary supports, show that the present solution is capable of dealing with complicated interval cavity shapes of sequential shallow tunnelling. Then the present solution can thereby be degenerated to adapt more simple cavity shapes, for example, the top heading and bench method in Fig. 2b, where

temporary supports may be not necessary. Therefore, the present solution is suitable for sequential shallow tunnelling methods that need no temporary supports without solution modification. The numerical cases in Sections 4 and 5, which certainly deviate from tunnel engineering fact without consideration of temporary supports, are deliberately conducted to demonstrate the significant theoretical improvements of present solution.

(2) Sequential excavation generally occurs with three-dimensional effect of tunnel face, which is not considered in the present solution. Thus, the stress and displacement fields computed by the present solution would deviate from real-world stress and displacement fields to a certain extent. To be conservative and to ensure construction safety, the present solution can be only used as very preliminary estimation of sequential shallow tunnelling.

(3) As pointed out in Section 5.4, no accumulative displacement can be computed via present solution owing to the simple elasticity assumption of geomaterial. Thus, the present solution should be further investigated and improved with time-dependent assumptions of geomaterial, such as viscoelasticity, to be more adaptive to real-world sequential tunnel excavation.

(4) The thin orthogonal grid in Fig. 5c and residual stress errors in Fig. 7c indicate a possible weakness of the present solution that the stress and displacement for sequential excavation stage of shallow tunnels with concave cavity may be inaccurate. For computation and design of concave cavity, the present solution may be not suitable.

7. Conclusions

This paper proposes a new complex variable solution on sequential shallow tunnelling in gravitational geomaterial with reasonable far-field displacement by incorporating with a new bidirectional stepwise conformal mapping scheme consisting of Charge Simulation Method and Complex Dipole Simulation Method. In the proposed solution, the sequential shallow tunnelling procedure is mathematically disassembled into parallel independent shallow tunnelling problems in a non-iterative manner to seek similar pattern of mixed boundary conditions and solution procedure, according to assumption of elasticity and small deformation. The mixed boundary conditions are transformed into a homogeneous Riemann-Hilbert problem, which is subsequently solved to obtain stress and displacement field in geomaterial. Via comparisons with corresponding finite element solution, the bidirectional stepwise conformal mapping scheme and the proposed solution are both sufficiently validated. A final parametric investigation shows several possible applications of the proposed solution in sequential shallow tunnelling with certain engineering recommendations.

Acknowledgements

This study is financially supported by the Fujian Provincial Natural Science Foundation of China (Grant No. 2022J05190), the Scientific Research Foundation of Fujian University of Technology (Grant No. GY-Z20094 and GY-H-22050), and the National Natural Science Foundation of China (Grant No. 52178318). The authors would like to thank Ph.D. Yiqun Huang for his suggestion on this study.

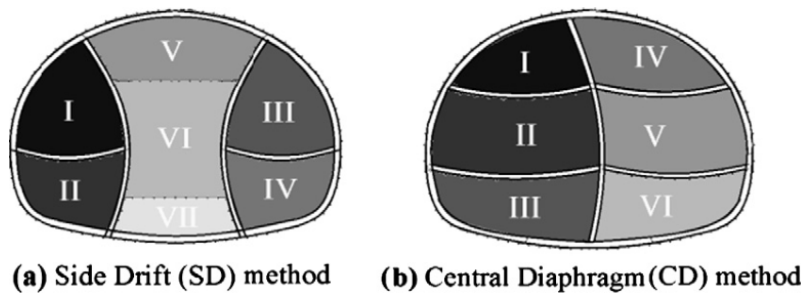
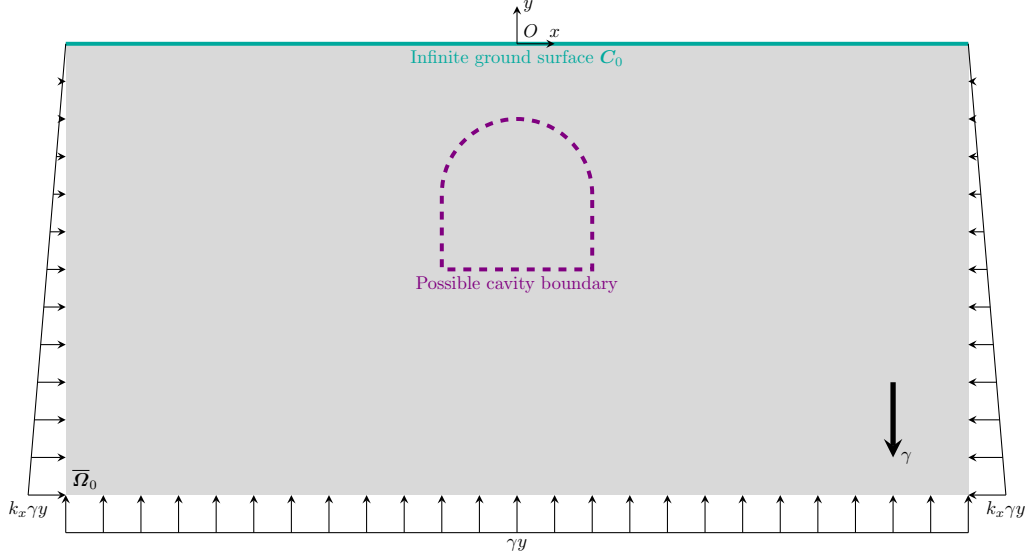


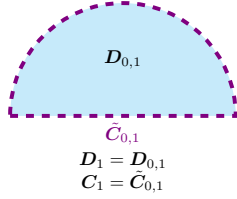
Figure 1: Typical sequential shallow excavation schemes with liners and temporary supports in Ref [1]

(a) Geomaterial before excavation and possible cavity boundary

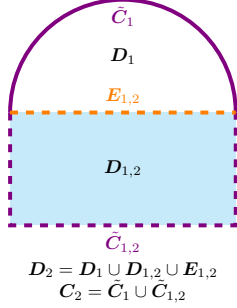


(b) Top heading and bench method
(No temporary supports needed)

(b-1) Stage-1 excavation

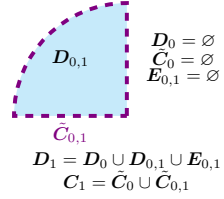


(b-2) Stage-2 excavation

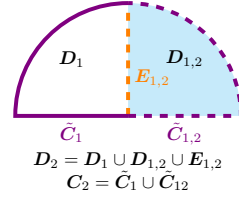


(c) Upper half vertical subdivision method
(Temporary supports not considered)

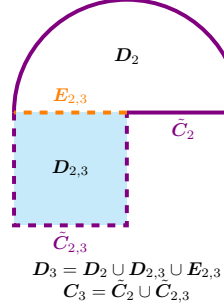
(c-1) Stage-1 excavation



(c-1) Stage-2 excavation



(c-3) Stage-3 excavation



(c-4) Stage-4 excavation

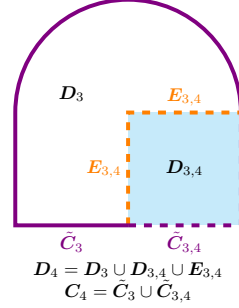


Figure 2: Geomaterial before excavation and two possible sequential excavation schemes

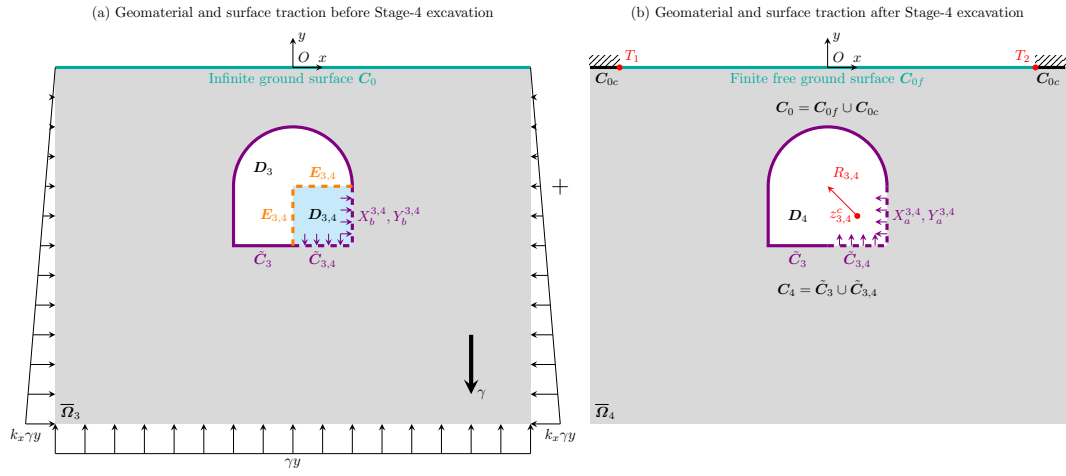


Figure 3: Boundary conditions of Stage-4 excavation of example in Fig. 2c

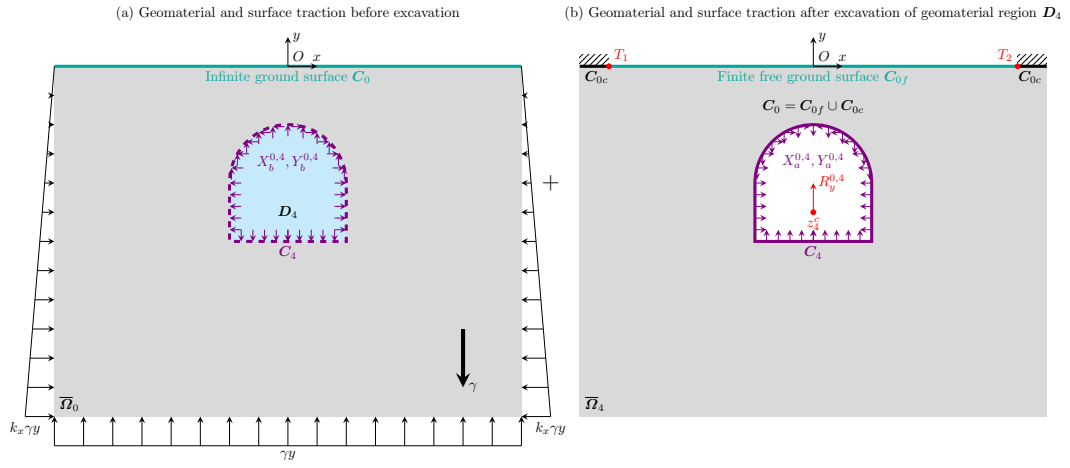


Figure 4: Boundary conditions of non-iterative excavation scheme of example in Fig. 3

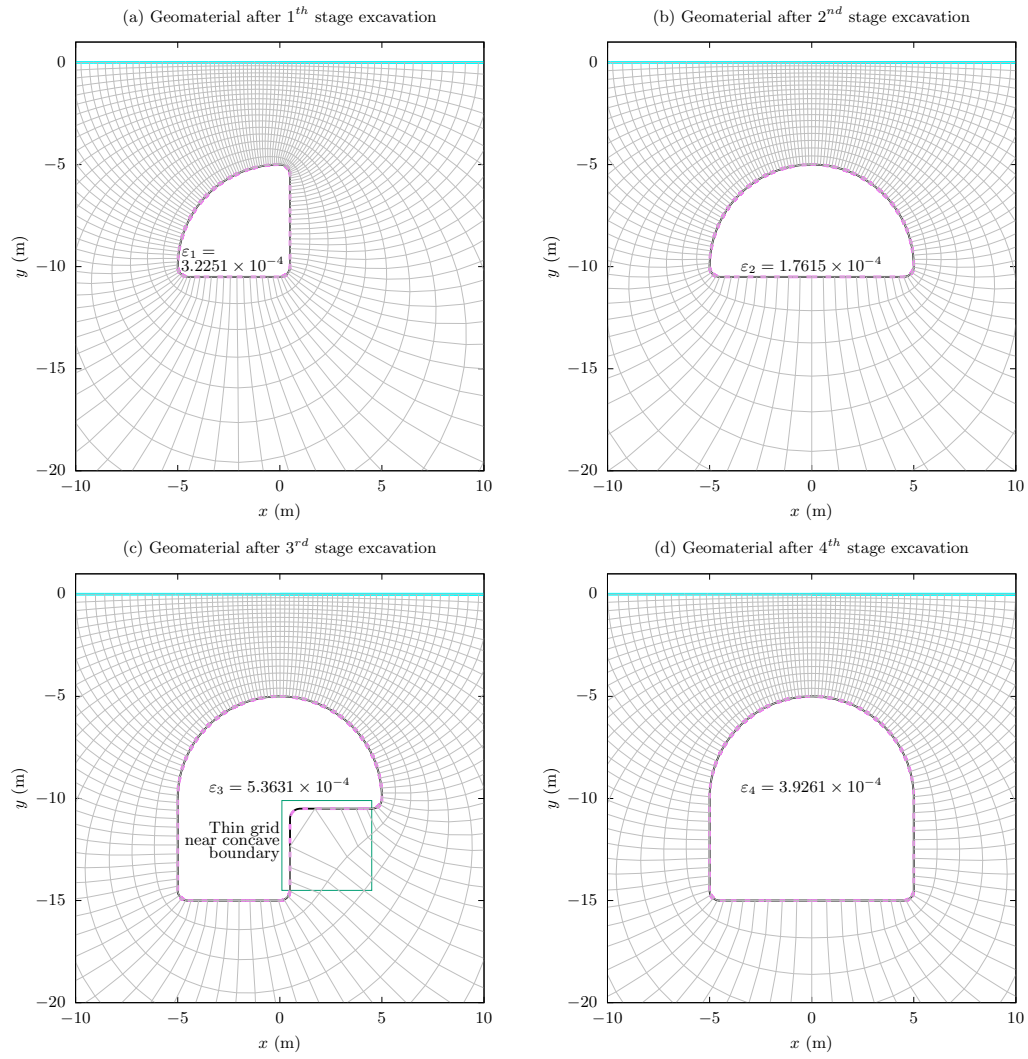
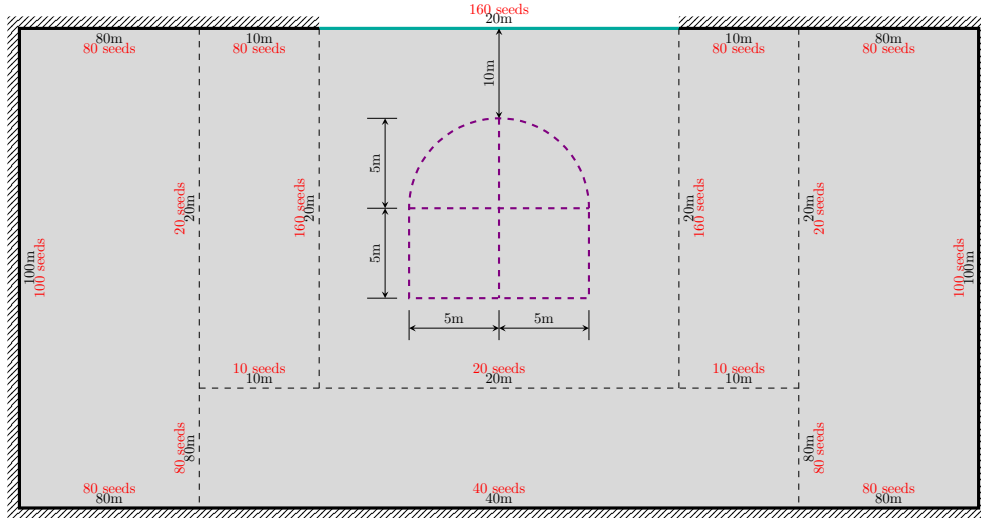
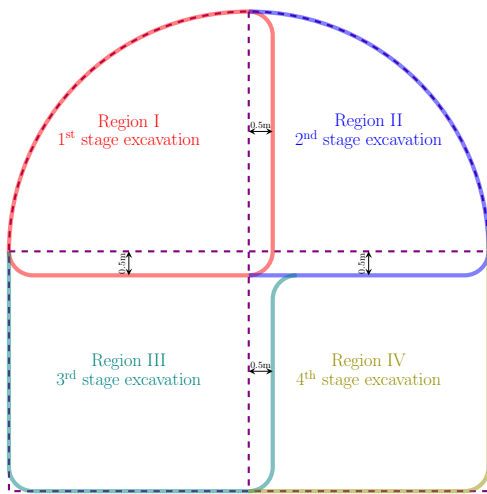


Figure 5: Curvilinear grids of backward conformal mapping of geomaterial for four excavation stages

(a) Schematic diagram of geometry and meshing strategy of finite element solution (102499 CPR4R elements)



(b) Detailed cavity geometry of 4-stage excavation



(c) Meshing near cavity of 4-stage excavation

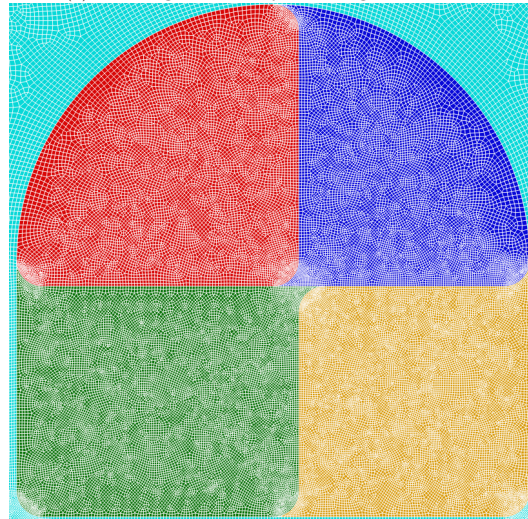


Figure 6: Geometry and meshing scheme of the finite element solution

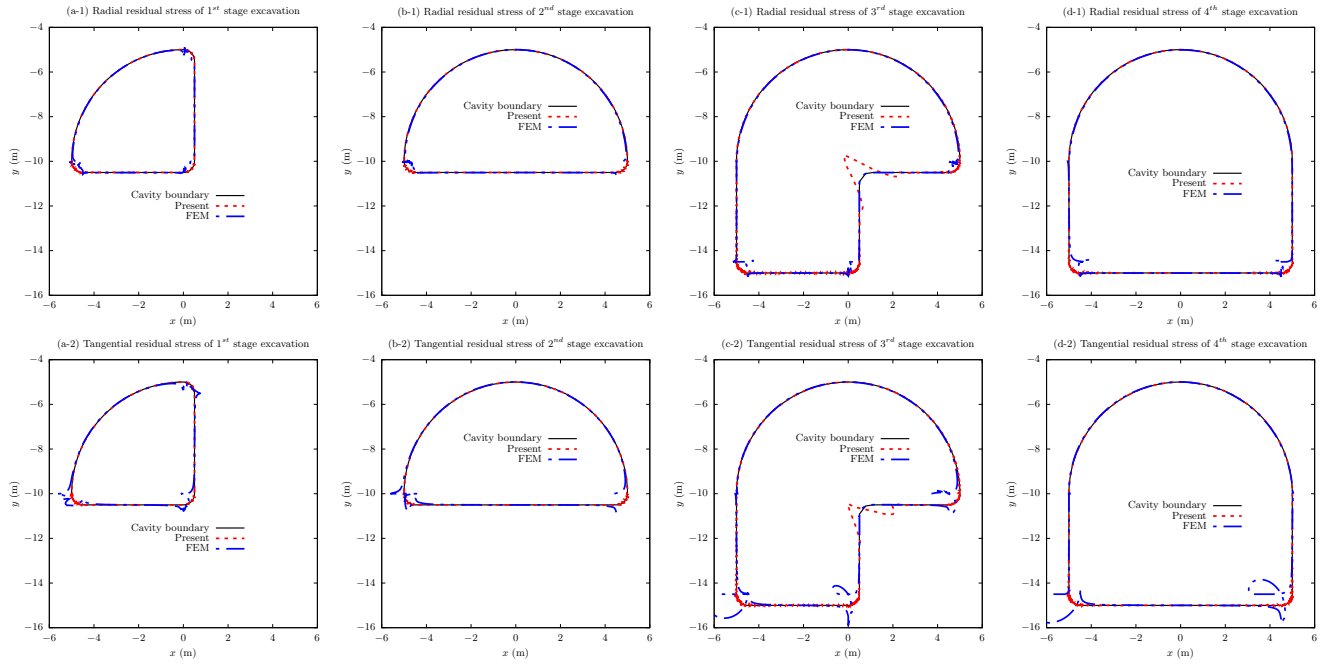


Figure 7: Comparisons of residual stress components along cavity boundaries of four excavation stages between present solution and finite element solution

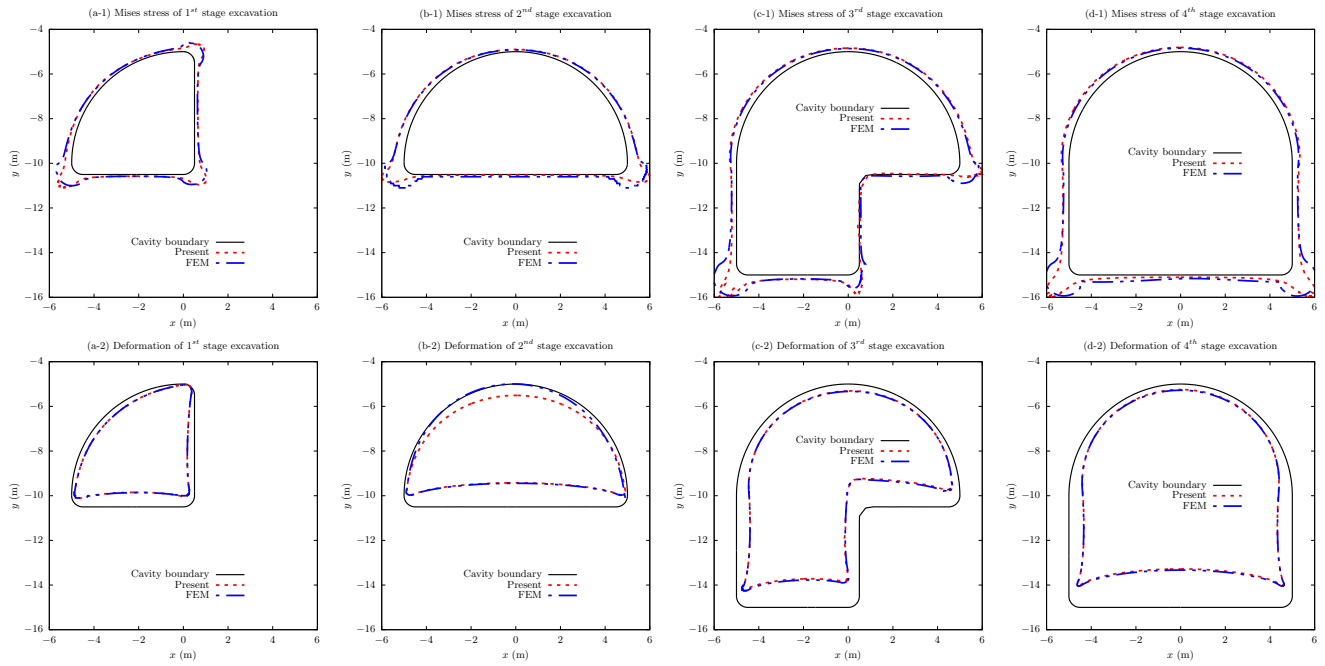


Figure 8: Comparisons of Mises stress and deformation along cavity boundaries of four excavation stages between present solution and finite element solution

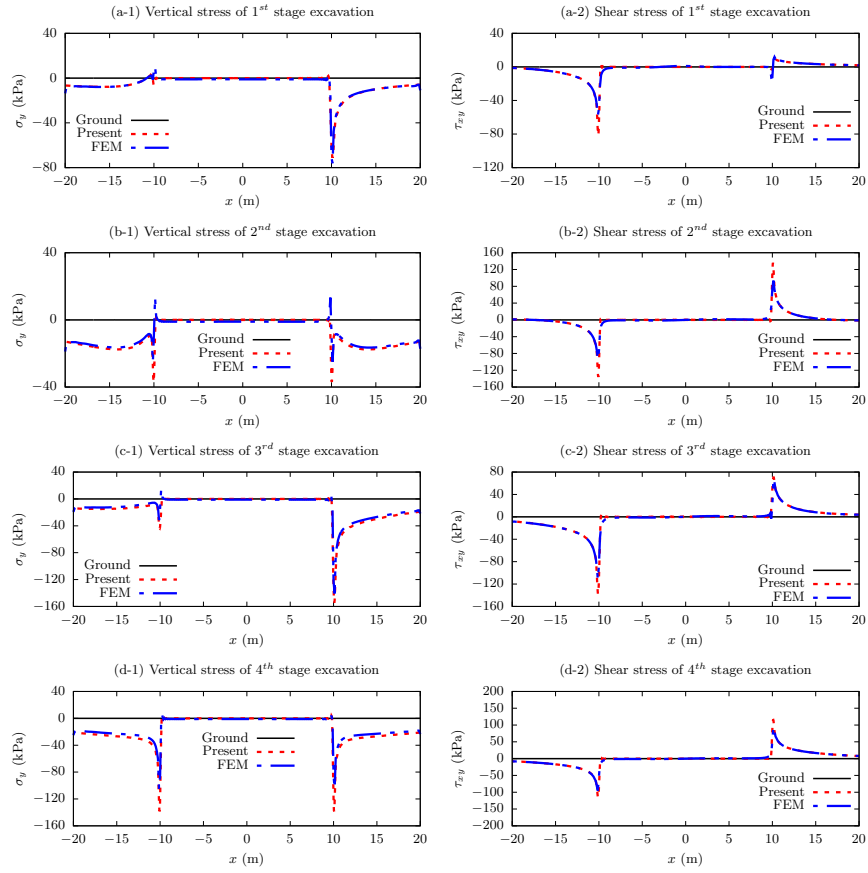


Figure 9: Comparisons of vertical and shear stress components along ground surface of four excavation stages between present solution and finite element solution

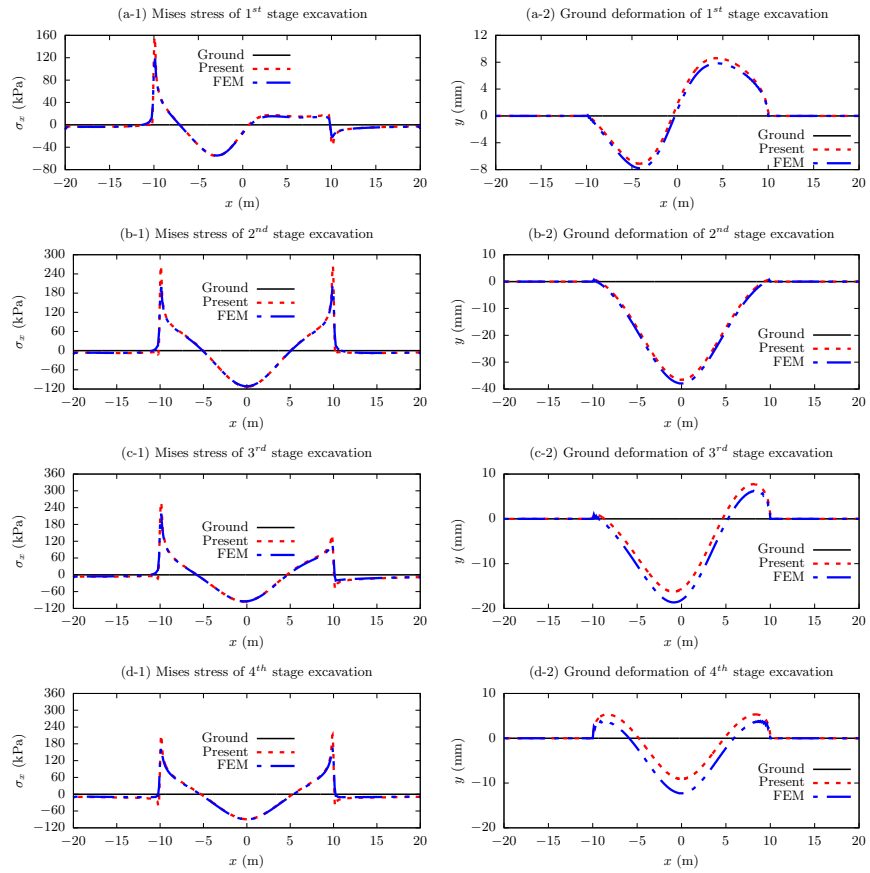


Figure 10: Comparisons of horizontal stress and deformation along ground surface of four excavation stages between present solution and finite element solution

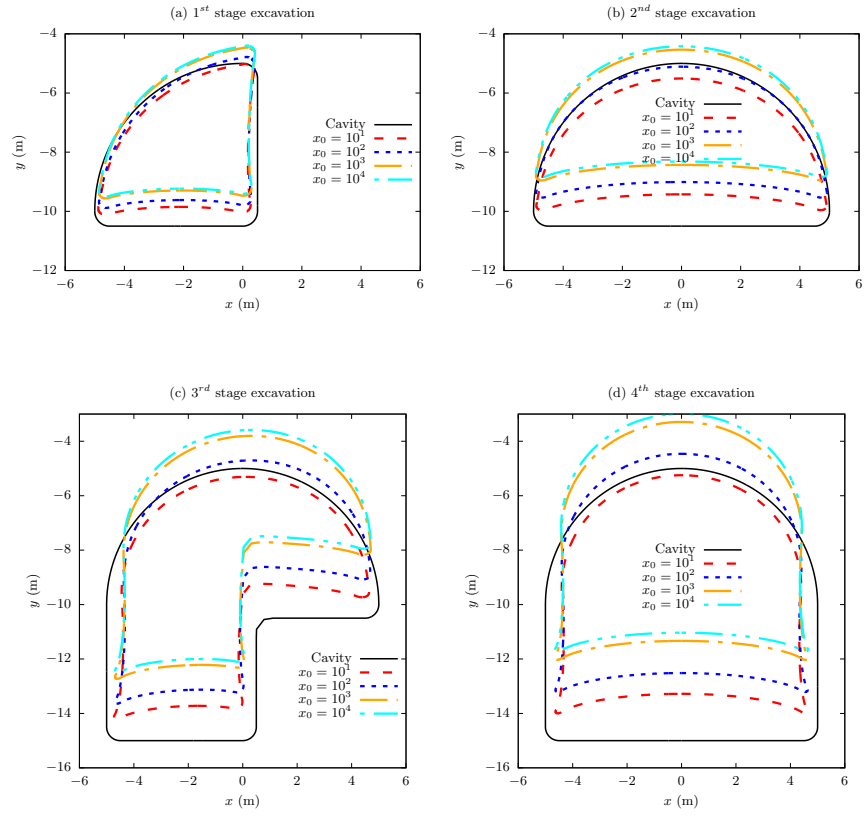


Figure 11: Cavity deformation (magnified by 10^2 times) against joint point coordinate x_0 for four excavation stages

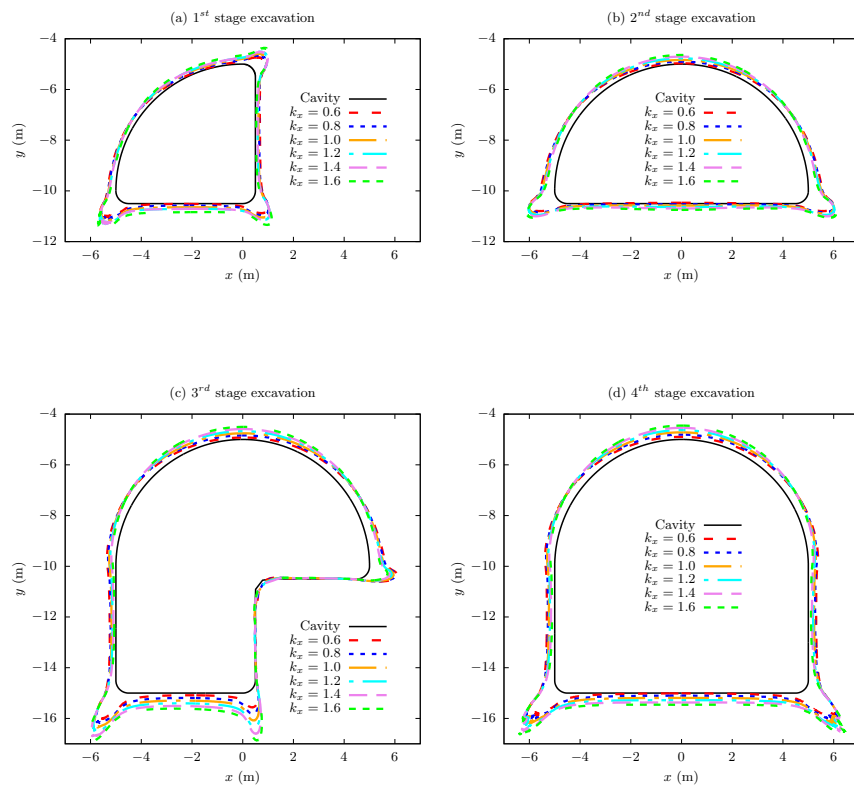


Figure 12: Mises stress along cavity boundary (reduced by 10^{-3}) against lateral coefficient k_x for four excavation stages

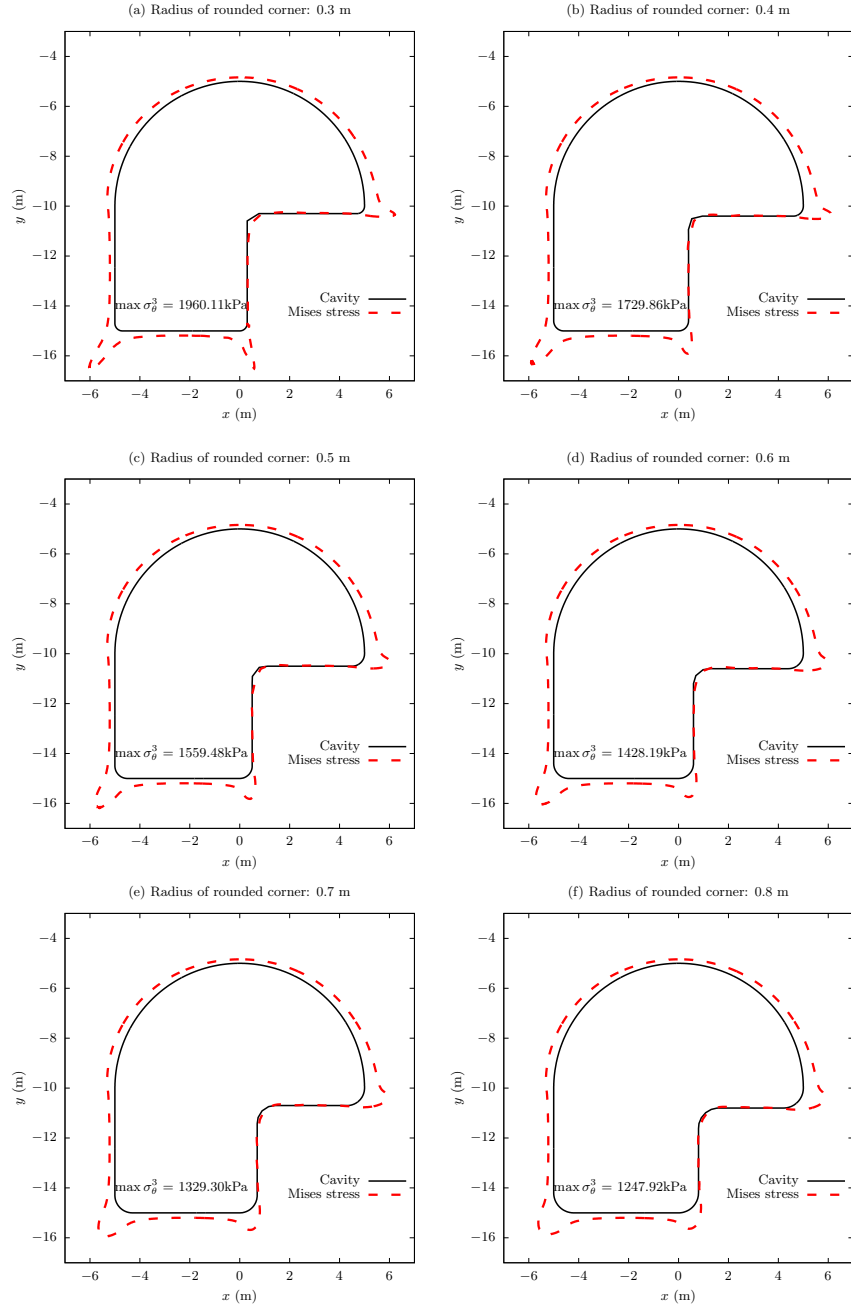


Figure 13: Mises stress along cavity boundary (reduced by 10^{-3}) of different radii of rounded corner for the 3th-stage excavation (maximum Mises stresses located at the left bottom corner)

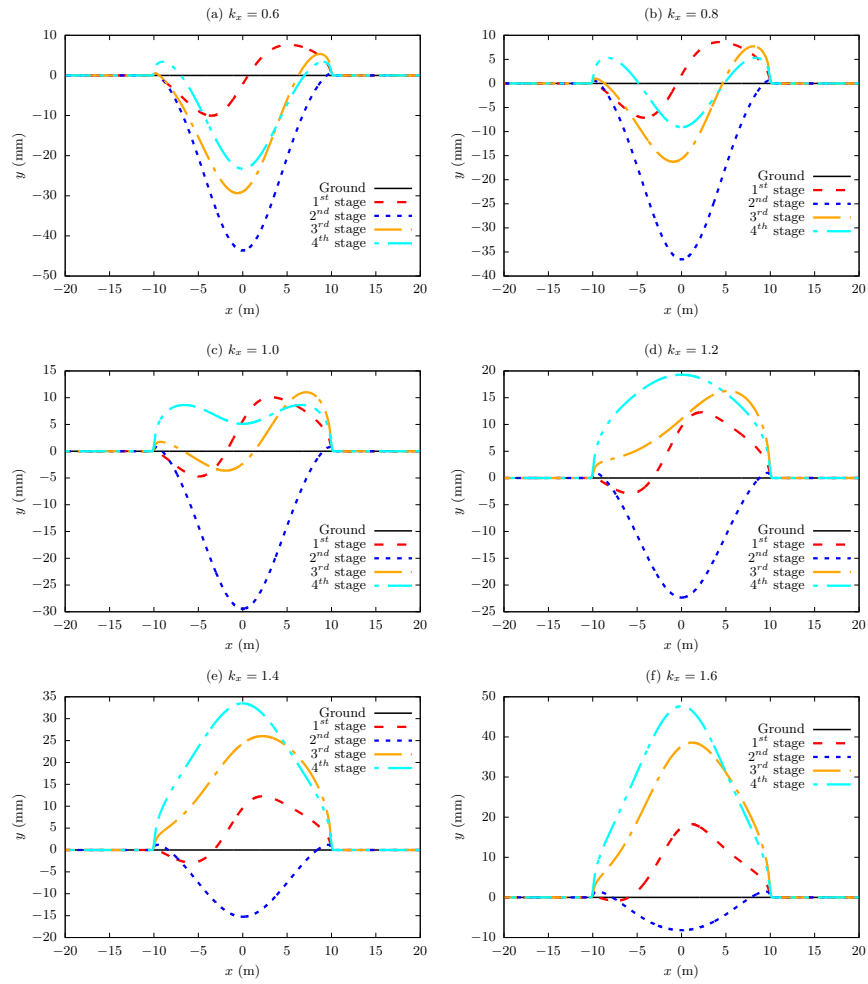


Figure 14: Deformation along ground surface for four excavation stages of different lateral coefficient k_x

Appendix A. Bidirectional conformal mapping

The geomaterials $\overline{\Omega}_j$ ($j = 1, 2, 3, \dots, n$) after excavation are lower half planes containing corresponding cavities of arbitrary shapes D_j , which are doubly-connected regions and can be bidirectionally mapped onto unit annuli $\overline{\omega}_j$ using the two-step mapping scheme in our previous study [35], respectively. Since the theory of such bidirectional conformal mapping has been elaborated in detail in Ref [35], the mapping scheme below only illustrates necessary numerical procedure for conciseness. Comparing to existing mapping schemes [39, 26, 40, 41], the proposed bidirectional conformal mapping has the following advantages: (1) Good adaptivity for a lower half plane containing an irregular and asymmetrical cavity; (2) Fast computation of solving a pair of linear systems below; (3) Closed logic to provide both forward and backward conformal mappings for mathematical rigor.

Appendix A.1. Mapping scheme

The first step is to bidirectionally map the geomaterial $\overline{\Omega}_j$ in the physical plane $z = x + iy$ onto interval annuli $\overline{\Omega}_j^w$ in interval mapping plane $w_j = \Re w_j + i\Im w_j$ using the following mapping schemes as

$$w_j = w_j(z) = \beta_j \frac{z - z_c^j}{z - \bar{z}_c^j}, \quad z \in \overline{\Omega}_j \quad (\text{A.1a})$$

$$z = z_j(w_j) = \frac{w_j \bar{z}_c^j - \beta_j z_c^j}{w_j - \beta_j}, \quad w_j \in \overline{\Omega}_j^w \quad (\text{A.1b})$$

where β_j denotes the exterior radius of the interval mapping annulus $\overline{\Omega}_j^w$, which should be given before-hand.

Via Eq. (A.1), the finite free segment $C_{0f,j}$ and far-field segment $C_{0c,j}$ of the ground surface $C_{0,j}$ in the physical plane $z = x + iy$ are bidirectionally mapped onto free arc segment $c_{0f,j}^w$ and constrained arc segment $c_{0c,j}^w$ of the exterior boundary $c_{0,j}^w = c_{0f,j}^w \cup c_{0c,j}^w$ in the interval mapping plane $w_j = \Re w_j + i\Im w_j$, respectively. The joint points T_1 and T_2 connecting segments $C_{0f,j}$ and $C_{0c,j}$ in the physical plane $z = x + iy$ are bidirectionally mapped onto corresponding joint points $t_{1,j}^w$ and $t_{2,j}^w$ connecting arc segments $c_{0f,j}^w$ and $c_{0c,j}^w$ in the interval mapping plane $w_j = \Re w_j + i\Im w_j$, respectively. The cavity boundary C_j in the physical plane $z = x + iy$ is bidirectionally mapped onto c_j^w in the interval mapping plane $w_j = \Re w_j + i\Im w_j$. Figs. A-1a and A-1b graphically and schematically show the bidirectional conformal mapping in Eq. (A.1) for the example in Fig. 4b.

The second step is to bidirectionally map the interval annulus $\overline{\Omega}_j^w$ in the interval mapping plane $w_j = \Re w_j + i\Im w_j$ onto corresponding unit mapping annulus $\overline{\omega}_j$ of interior radius α_j in the mapping plane $\zeta_j = \rho_j \cdot e^{i\theta_j}$. The forward and backward conformal mappings of second-step bidirectional conformal mapping can be respectively expressed using Charge Simulation Method [37, 42, 35] and Complex Dipole Simulation Method [38, 35] as

$$\zeta_j = \zeta_j(w_j) = \frac{w_j - w_j^c}{w_j^\beta - w_j^c} \cdot \exp \left[\sum_{k=1}^{N_0} P_{j,k} \ln \frac{w_j - U_{j,k}}{w_j^\beta - U_{j,k}} + \sum_{k=1}^{N_j} Q_{j,k} \ln \frac{w_j - V_{j,k}}{w_j^\beta - V_{j,k}} \right] \quad (\text{A.2a})$$

$$w_j = w_j(\zeta_j) = \sum_{k=1}^{N_0} \frac{p_{j,k}}{\zeta_j - \eta_{j,k}} + \sum_{k=1}^{N_j} \frac{q_{j,k}}{\zeta_j - \mu_{j,k}} \quad (\text{A.2b})$$

where w_j^c denotes arbitrary point within interior boundary c_j^w of the interval mapping annulus $\overline{\Omega}_j^w$ for fixed point normalization; w_j^β denotes arbitrary point along exterior boundary $c_{0,j}$ (the radius is

β_j) for rotation normalization, and generally can take the coordinate $w_j^\beta = \beta$ for simplicity; $P_{j,k}$ and $Q_{j,k}$ denote *charges* of Charge Simulation Method, and are real variables to be determined by Eq. (A.5); $U_{j,k}$ and $V_{j,k}$ denote *charge points* of Charge Simulation Method, and are complex coefficients determined by Eq. (A.3); $p_{j,k}$ and $q_{j,k}$ are *charges* of Complex Dipole Simulation Method, and are complex variables to be determined by Eq. (A.6); $\eta_{j,k}$ and $\mu_{j,k}$ are *charge points* of Complex Dipole Simulation Method, and are complex coefficients determined by Eq. (A.4); N_0 and N_j denote quantities of charge points along exterior boundary $\mathbf{c}_{0,j}^w$ (or $\mathbf{c}_{0,j}$) and interior boundary \mathbf{c}_j^w (or \mathbf{c}_j), respectively.

Via Eq. (A.2), the free arc segment $\mathbf{c}_{0f,j}^w$ and constrained arc segment $\mathbf{c}_{0c,j}^w$ of exterior boundary \mathbf{c}_{0f}^w in the interval mapping plane $w_j = \Re w_j + i\Im w_j$ are bidirectionally mapped onto free segment $\mathbf{c}_{0f,j}$ and constrained arc segment $\mathbf{c}_{0c,j}$ of unit exterior boundary $\mathbf{c}_{0,j} = \mathbf{c}_{0f,j} \cup \mathbf{c}_{0c,j}$ in the mapping plane $\zeta_j = \rho_j \cdot e^{i\theta_j}$, respectively. The joint points $t_{1,j}^w$ and $t_{2,j}^w$ connecting arc segments $\mathbf{c}_{0f,j}^w$ and $\mathbf{c}_{0c,j}^w$ in the interval mapping plane $w = \Re w + i\Im w$ are bidirectionally mapped onto corresponding joint points $t_{1,j}$ and $t_{2,j}$ connecting unit arc segments $\mathbf{c}_{0f,j}$ and $\mathbf{c}_{0c,j}$ in the mapping plane $\zeta_j = \rho_j \cdot e^{i\theta_j}$, respectively. The possibly noncircular interior boundary \mathbf{c}_j^w in the interval mapping plane $w = \Re w + i\Im w$ is bidirectionally mapped onto the circular interior boundary \mathbf{c}_j of radius α_j . The interior and exterior regions of boundary $\mathbf{c}_{0,j}$ are denoted by $\omega_{0,j}^+$ and $\omega_{0,j}^-$, respectively. Figs. A-1b and A-1c graphically and schematically show the subsequent bidirectional conformal mapping in Eq. (A.2) for the example in Fig. A-1a.

The charge points of Charge Simulation Method can be given as

$$\begin{cases} U_{j,k} = w_{j,k}^0 + K_j^0 \cdot H_{j,k}^0 \cdot \exp(i\Theta_{j,k}^0) \\ H_{j,k}^0 = \frac{1}{2} (|w_{j,k+1}^0 - w_{j,k}^0| + |w_{j,k}^0 - w_{j,k-1}^0|), \quad k = 1, 2, 3, \dots, N_0 \\ \Theta_{j,k}^0 = \arg(w_{j,k+1}^0 - w_{j,k-1}^0) - \frac{\pi}{2} \end{cases} \quad (\text{A.3a})$$

$$\begin{cases} V_{j,k} = w_{j,k}^1 + K_j^1 \cdot H_{j,k}^1 \cdot \exp(i\Theta_{j,k}^1) \\ H_{j,k}^1 = \frac{1}{2} (|w_{j,k+1}^1 - w_{j,k}^1| + |w_{j,k}^1 - w_{j,k-1}^1|), \quad k = 1, 2, 3, \dots, N_j \\ \Theta_{j,k}^1 = \arg(w_{j,k+1}^1 - w_{j,k-1}^1) - \frac{\pi}{2} \end{cases} \quad (\text{A.3b})$$

where $w_{j,k}^0$ and $w_{j,k}^1$ denote *collocation points* of Charge Simulation Method distributed along exterior boundary $\mathbf{c}_{0,j}^w$ and interior boundary \mathbf{c}_j^w of the interval mapping region $\overline{\Omega}_j^w$, respectively, and the selection schemes can be seen in Appendix A.2; K_j^0 and K_j^1 denote *assignment factors* of Charge Simulation Method for collocation points along exterior boundary $\mathbf{c}_{0,j}^w$ and interior boundary \mathbf{c}_j^w , respectively; $H_{j,k}^0$ and $H_{j,k}^1$ denote distances between charge points and corresponding collocation points along exterior boundary $\mathbf{c}_{0,j}^w$ and interior boundary \mathbf{c}_j^w , respectively; $\Theta_{j,k}^0$ and $\Theta_{j,k}^1$ denote outward normal angles pointing from collocation points to corresponding charge points along exterior boundary $\mathbf{c}_{0,j}^w$ and interior boundary \mathbf{c}_j^w , respectively.

The charge points of Complex Dipole Simulation Method can be given as

$$\begin{cases} \eta_{j,k} = \zeta_{j,k}^0 + k_j^0 \cdot h_{j,k}^0 \cdot \exp(i\vartheta_{j,k}^0) \\ h_{j,k}^0 = \frac{1}{2} (|\zeta_{j,k+1}^0 - \zeta_{j,k}^0| + |\zeta_{j,k}^0 - \zeta_{j,k-1}^0|), \quad k = 1, 2, 3, \dots, N_0 \\ \vartheta_{j,k}^0 = \arg(\zeta_{j,k+1}^0 - \zeta_{j,k-1}^0) - \frac{\pi}{2} \end{cases} \quad (\text{A.4a})$$

$$\begin{cases} \mu_{j,k} = \zeta_{j,k}^1 + k_j^1 \cdot h_{j,k}^1 \cdot \exp(i\vartheta_{j,k}^1) \\ h_{j,k}^1 = \frac{1}{2} (|\zeta_{j,k+1}^1 - \zeta_{j,k}^1| + |\zeta_{j,k}^1 - \zeta_{j,k-1}^1|), \quad k = 1, 2, 3, \dots, N_j \\ \vartheta_{j,k}^1 = \arg(\zeta_{j,k+1}^1 - \zeta_{j,k-1}^1) - \frac{\pi}{2} \end{cases} \quad (\text{A.4b})$$

where $\zeta_{j,k}^0$ and $\zeta_{j,k}^1$ denote *collocation points* of Complex Dipole Simulation Method distributed along exterior boundary $\mathbf{c}_{0,j}$ and interior boundary \mathbf{c}_j of the interval mapping region $\overline{\omega}_j$, respectively, and are determined by Eq. (A.7); k_j^0 and k_j^1 denote *assignment factors* of Complex Dipole Simulation Method for collocation points along exterior boundary $\mathbf{c}_{0,j}$ and interior boundary \mathbf{c}_j , respectively; $h_{j,k}^0$ and $h_{j,k}^1$ denote distances between charge points and corresponding collocation points along exterior boundary $\mathbf{c}_{0,j}$ and interior boundary \mathbf{c}_j , respectively; $\vartheta_{j,k}^0$ and $\vartheta_{j,k}^1$ denote outward normal angles pointing from collocation points to corresponding charge points along exterior boundary $\mathbf{c}_{0,j}$ and interior boundary \mathbf{c}_j , respectively.

With the charge points in Eq. (A.3), the charges in Eq. (A.2a) can be determined as

$$\sum_{k=1}^{N_0} \ln \left| \frac{w_{j,i}^0 - U_{j,k}}{w_j^\beta - U_{j,k}} \right| \cdot P_{j,k} + \sum_{k=1}^{N_j} \ln \left| \frac{w_{j,i}^0 - V_{j,k}}{w_j^\beta - V_{j,k}} \right| \cdot Q_{j,k} - \ln r_e = -\ln \left| \frac{w_{j,k}^0 - w_j^c}{w_j^\beta - w_j^c} \right|, \quad i = 1, 2, 3, \dots, N_0 \quad (\text{A.5a})$$

$$\sum_{k=1}^{N_0} \ln \left| \frac{w_{j,i}^1 - U_{j,k}}{w_j^\beta - U_{j,k}} \right| \cdot P_{j,k} + \sum_{k=1}^{N_j} \ln \left| \frac{w_{j,i}^1 - V_{j,k}}{w_j^\beta - V_{j,k}} \right| \cdot Q_{j,k} - \ln \alpha_j = -\ln \left| \frac{w_{j,k}^1 - w_j^c}{w_j^\beta - w_j^c} \right|, \quad i = 1, 2, 3, \dots, N_j \quad (\text{A.5b})$$

$$\sum_{k=1}^{N_0} P_{j,k} = -1 \quad (\text{A.5c})$$

$$\sum_{k=1}^{N_j} Q_{j,k} = 0 \quad (\text{A.5d})$$

Eq. (A.5) contains $N_0 + N_j + 2$ to-be-determined real variables and real linear equations to form simultaneous real linear system, and unique solution can be obtained.

With the charge points in Eq. (A.4), the charges in Eq. (A.2b) can be determined as

$$\sum_{k=1}^{N_0} \frac{p_{j,k}}{\zeta_{j,i}^0 - \eta_{j,k}} + \sum_{k=1}^{N_j} \frac{q_{j,k}}{\zeta_{j,i}^0 - \mu_{j,k}} = w_{j,i}^0, \quad i = 1, 2, 3, \dots, N_0 \quad (\text{A.6a})$$

$$\sum_{k=1}^{N_0} \frac{p_{j,k}}{\zeta_{j,i}^1 - \eta_{j,k}} + \sum_{k=1}^{N_j} \frac{q_{j,k}}{\zeta_{j,i}^1 - \mu_{j,k}} = w_{j,i}^1, \quad i = 1, 2, 3, \dots, N_j \quad (\text{A.6b})$$

where

$$\zeta_{j,i}^0 = \zeta_j(w_{j,i}^0), \quad i = 1, 2, 3, \dots, N_0 \quad (\text{A.7a})$$

$$\zeta_{j,i}^1 = \zeta_j(w_{j,i}^1), \quad i = 1, 2, 3, \dots, N_j \quad (\text{A.7b})$$

Eq. (A.7) is computed using Eq. (A.2a'). Eq. (A.6) contains $N_0 + N_j$ to-be-determined complex variables and complex linear equations to form simultaneous complex linear system, and unique solution can be obtained.

In summary, the bidirectional conformal mapping in Eq. (A.2) can be determined by the linear systems in Eqs. (A.5) and (A.6) with auxiliary supports of Eqs. (A.3), (A.4), and (A.7), except for the before-hand determination of collocation points $w_{j,k}^0$ and $w_{j,k}^1$, which would be given in Appendix A.2 with certain numerical principles.

Appendix A.2. Numerical schemes

The collocation point selection of $w_{j,k}^0$ and $w_{j,k}^1$ in Eq. (A.3) should be suitable to guarantee the analyticity and accuracy of the backward conformal mapping in Eq. (A.2b). The collocation points along boundaries $\mathbf{c}_{0,j}^w$ and \mathbf{c}_j^w of the interval mapping annulus $\overline{\Omega}_j^w$ should be distributed as uniformly as possible, and sharp corners should be eliminated to avoid boundary singularities [43, 44]. Therefore, we should first ensure that no sharp corners exist along the cavity boundary \mathbf{C}_j in the physical geomaterial region $\overline{\Omega}_j$. In Figs. 2-4 and A-1a, the sharp corners of cavity boundaries for sequential shallow tunnelling are kept merely due to convenience of schematic plotting. In practical tunnel engineering, sharp corners are generally rounded on purpose to avoid stress concentration. Therefore, the sharp corners in this paper do not exist, and Fig. A-2 graphically shows the replacement of rounded corners with sharp corners for the example of Fig. A-1a.

Therefore, the rounded corners guarantee the continuity and analyticity of the cavity boundary \mathbf{C}_j in the physical plane $z = x + iy$. Subsequently, via the first-step conformal mapping in Eq. (A.1), the exterior circular boundary $\mathbf{c}_{0,j}^w$ (mapped from the straight ground surface \mathbf{C}_0) and interior boundary \mathbf{c}_j^w in the interval mapping annulus $\overline{\Omega}_j^w$ (possibly not circular) would contain no sharp corners, so that the continuity of the outward normal angles $\Theta_{j,k}^0$ and $\Theta_{j,k}^1$ in Eq. (A.3) would be potentially guaranteed by mandatorily setting the following numerical principle as

$$\max \left[\max_{1 \leq k \leq N_0} |\arg(w_{j,k+1}^0 - w_{j,k}^0)|, \max_{1 \leq k \leq N_j} |\arg(w_{j,k+1}^1 - w_{j,k}^1)| \right] \leq 10^\circ \quad (\text{A.8a})$$

Moreover, the quantity of collocation points should be large enough, thus, the following numerical principle is mandatorily set as

$$\max \left[\max_{1 \leq k \leq N_0} \frac{|w_{j,k+1}^0 - w_{j,k}^0|}{\sum_{l=1}^{N_0} |w_{j,l}^0 - w_{j,l}^0|}, \max_{1 \leq k \leq N_j} \frac{|w_{j,k+1}^1 - w_{j,k}^1|}{\sum_{l=1}^{N_j} |w_{j,l}^1 - w_{j,l}^1|} \right] \leq 10^{-2} \quad (\text{A.8b})$$

Eq. (A.8) is based on the numerical principles proposed in our previous study [35], and controls the varying angle and distance between adjacent collocation points along boundaries $\mathbf{c}_{0,j}^w$ and \mathbf{c}_j^w .

Additionally, Eq. (A.2a) should be slightly modified after solving the charges by Eq. (A.5) to guarantee the single-valuedness of arguments without changing the principal values of the computation results [42, 35] as

$$\zeta_j = \zeta_j(w_j) = \frac{w_j - w_j^c}{w_j^\beta - w_j^c} \cdot \exp \left[\begin{aligned} & \sum_{k=1}^{N_0} P_{j,k} \left(\ln \frac{w_j - U_{j,k}}{w_{j,0} - U_{j,k}} - \ln \frac{w_j^\beta - U_{j,k}}{w_{j,0} - U_{j,k}} \right) \\ & + \sum_{k=1}^{N_j} Q_{j,k} \left(\ln \frac{w_j - V_{j,k}}{w_j - w_j^c} - \ln \frac{w_j^\beta - V_{j,k}}{w_j^\beta - w_j^c} \right) \end{aligned} \right] \quad (\text{A.2a}')$$

where $w_{j,0}$ denote an arbitrary point within interval mapping region $\overline{\Omega}_j^w$.

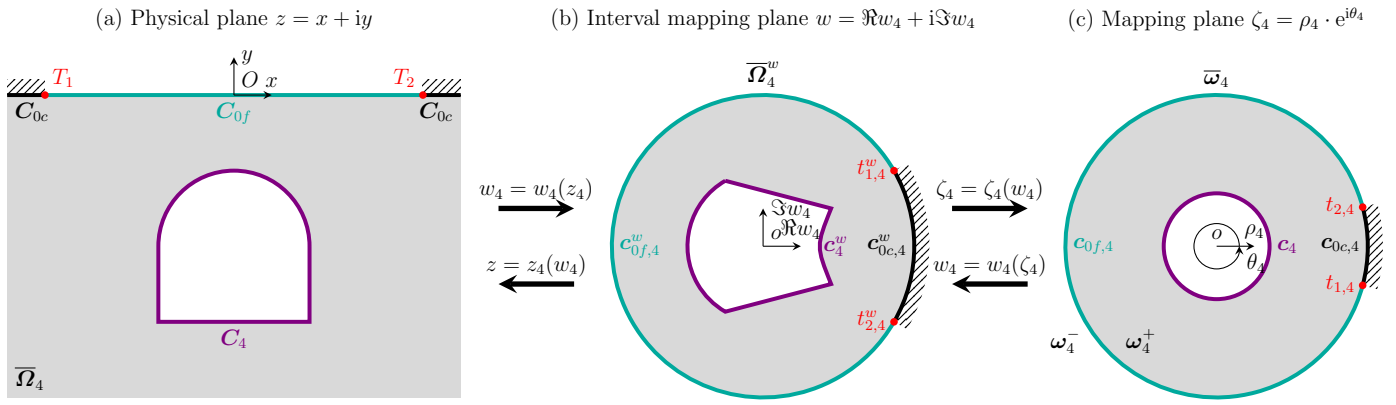


Figure A-1: Stepwise bidirectional conformal mapping – a schematic example for Fig. 4b

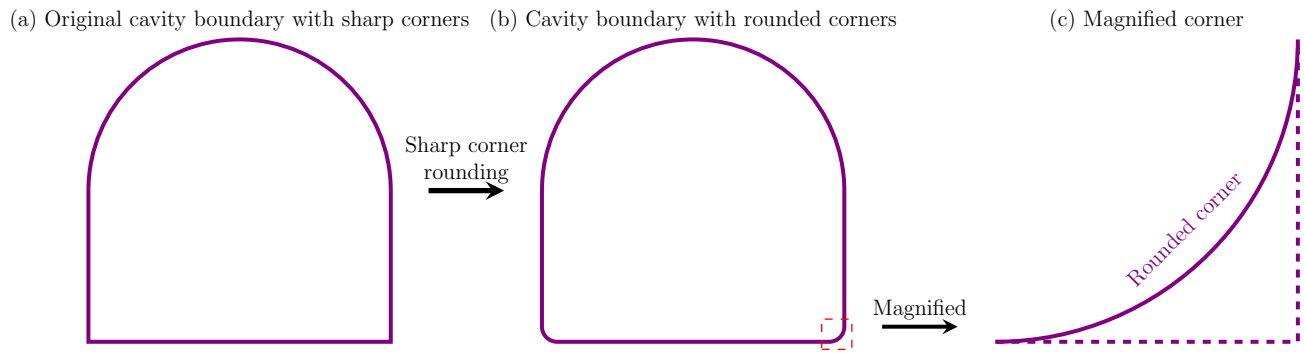


Figure A-2: Rounding of sharp corners – schematic diagram for the cavity boundary in Fig. A-1a

References

- [1] M. Sharifzadeh, F. Kolivand, M. Ghorbani, S. Yasrobi, Design of sequential excavation method for large span urban tunnels in soft ground—niayesh tunnel, *Tunn. Undergr. Space Technol.* 35 (2013) 178–188.
- [2] P. Li, Y. Zhao, X. Zhou, Displacement characteristics of high-speed railway tunnel construction in loess ground by using multi-step excavation method, *Tunn. Undergr. Space Technol.* 51 (2016) 41–55.
- [3] Q. Fang, X. Liu, D. Zhang, H. Lou, Shallow tunnel construction with irregular surface topography using cross diaphragm method, *Tunn. Undergr. Space Technol.* 68 (2017) 11–21.
- [4] C. Shi, C. Cao, M. Lei, Construction technology for a shallow-buried underwater interchange tunnel with a large span, *Tunn. Undergr. Space Technol.* 70 (2017) 317–329.
- [5] C. Cao, C. Shi, M. Lei, W. Yang, J. Liu, Squeezing failure of tunnels: a case study, *Tunn. Undergr. Space Technol.* 77 (2018) 188–203.
- [6] W. Liu, J. Chen, Y. Luo, L. Chen, Z. Shi, Y. Wu, Deformation behaviors and mechanical mechanisms of double primary linings for large-span tunnels in squeezing rock: a case study, *Rock Mech. Rock Eng.* 54 (2021) 2291–2310.
- [7] S. Zhou, L. Li, Z. An, H. Liu, G. Yang, P. Zhou, Stress-release law and deformation characteristics of large-span tunnel excavated with semi central diaphragm method, *KSCE J. Civil Eng.* 25 (2021) 2275–2284.
- [8] A. Verruijt, Deformations of an elastic plane with a circular cavity, *Int. J. Solids Struct.* 35 (21) (1997) 2795–2804.
- [9] A. Verruijt, A complex variable solution for a deforming circular tunnel in an elastic half-plane, *Int. J. Numer. Anal. Methods Geomech.* 21 (2) (1997) 77–89.
- [10] Z. Zhang, M. Huang, X. Xi, X. Yang, Complex variable solutions for soil and liner deformation due to tunneling in clays, *Int. J. Geomech.* 18 (7) (2018) 04018074.
- [11] H. Wang, X. Gao, L. Wu, M. Jiang, Analytical study on interaction between existing and new tunnels parallel excavated in semi-infinite viscoelastic ground, *Comput. Geotech.* 120 (2020) 103385.
- [12] Z. Zhang, Y. Pan, M. Zhang, X. Lv, K. Jiang, S. Li, Complex variable analytical prediction for ground deformation and lining responses due to shield tunneling considering groundwater level variation in clays, *Comput. Geotech.* 120 (2020) 103443.
- [13] Z. Zhang, M. Huang, Y. Pan, K. Jiang, Z. Li, S. Ma, Y. Zhang, Analytical prediction of time-dependent behavior for tunneling-induced ground movements and stresses subjected to surcharge loading based on rheological mechanics, *Comput. Geotech.* 129 (2021) 103858.
- [14] F. Kong, D. Lu, X. Du, C. Shen, Displacement analytical prediction of shallow tunnel based on unified displacement function under slope boundary, *Int. J. Numer. Anal. Methods Geomech.* 43 (1) (2019) 183–211.

- [15] D. Lu, F. Kong, X. Du, C. Shen, Q. Gong, P. Li, A unified displacement function to analytically predict ground deformation of shallow tunnel, *Tunn. Undergr. Space Technol.* 88 (2019) 129–143.
- [16] F. Kong, D. Lu, X. Du, X. Li, C. Su, Analytical solution of stress and displacement for a circular underwater shallow tunnel based on a unified stress function, *Ocean Eng.* 219 (2021) 108352.
- [17] H. Wang, L. Wu, M. Jiang, F. Song, Analytical stress and displacement due to twin tunneling in an elastic semi-infinite ground subjected to surcharge loads, *Int. J. Numer. Anal. Methods Geomech.* 42 (6) (2018) 809–828.
- [18] H. Wang, X. P. Chen, M. Jiang, F. Song, L. Wu, The analytical predictions on displacement and stress around shallow tunnels subjected to surcharge loadings, *Tunn. Undergr. Space Technol.* 71 (2018) 403–427.
- [19] L. Lin, Y. Lu, F. Chen, D. Li, B. Zhang, Analytic study of stress and displacement for shallow twin tunnels subjected to surcharge loads, *Appl. Math. Model.* 93 (2021) 485–508.
- [20] O. E. Strack, Analytic solutions of elastic tunneling problems, Ph.D. thesis, Delft University of Technology, Amsterdam (2002).
- [21] O. E. Strack, A. Verruijt, A complex variable solution for a deforming buoyant tunnel in a heavy elastic half-plane, *Int. J. Numer. Anal. Methods Geomech.* 26 (12) (2002) 1235–1252.
- [22] A. Verruijt, O. E. Strack, Buoyancy of tunnels in soft soils, *Géotech.* 58 (6) (2008) 513–515.
- [23] Q. Fang, H. Song, D. Zhang, Complex variable analysis for stress distribution of an underwater tunnel in an elastic half plane, *Int. J. Numer. Anal. Methods Geomech.* 39 (16) (2015) 1821–1835.
- [24] A. Lu, X. Zeng, Z. Xu, Solution for a circular cavity in an elastic half plane under gravity and arbitrary lateral stress, *Int. J. Rock Mech. Min. Sci.* 89 (2016) 34–42.
- [25] A. Lu, H. Cai, S. Wang, A new analytical approach for a shallow circular hydraulic tunnel, *Mecc.* 54 (1-2) (2019) 223–238.
- [26] G. Zeng, H. Cai, A. Lu, An analytical solution for an arbitrary cavity in an elastic half-plane, *Rock Mech. Rock Eng.* 52 (2019) 4509–4526.
- [27] A. Lu, G. Zeng, N. Zhang, A complex variable solution for a non-circular tunnel in an elastic half-plane, *Int. J. Numer. Anal. Methods Geomech.* 45 (12) (2021) 1833–1853.
- [28] G. Zeng, H. Wang, M. Jiang, Analytical solutions of noncircular tunnels in viscoelastic semi-infinite ground subjected to surcharge loadings, *Appl. Math. Model.* 102 (2022) 492–510.
- [29] G. Zeng, H. Wang, M. Jiang, Analytical stress and displacement of twin noncircular tunnels in elastic semi-infinite ground, *Comput. Geotech.* 160 (2023) 105520.
- [30] T. Fan, J. Wang, Z. Wang, Analytical solutions of elastic complex variables for tunnels with complicated shapes under geostress field, *Rock Mech. Rock Eng.* (2024) 1–21.

- [31] Y. Zhou, A. Lu, N. Zhang, An analytical solution for the orthotropic semi-infinite plane with an arbitrary-shaped hole, *Math. Mech. Solids* (2024) 10812865231225131.
- [32] L. Lin, F. Chen, X. Huang, Reasonable mechanical model on shallow tunnel excavation to eliminate displacement singularity caused by unbalanced resultant, *Appl. Math. Model.* 127 (2024) 396–431.
- [33] L. Lin, F. Chen, S. Lin, A new complex variable solution on noncircular shallow tunnelling with reasonable far-field displacement, *Comput. Geotech.* 166 (2024) 106008.
- [34] L. Lin, F. Chen, J. Zhuang, Complex variable solution on over-/under-break shallow tunnelling in gravitational geomaterial with reasonable far-field displacement, *Comput. Geotech.* 174 (2024) 106595.
- [35] L. Lin, F. Chen, C. Zheng, S. Lin, Complex variable solution on noncircular and asymmetrical tunnelling embedded by bidirectional conformal mapping incorporating charge simulation method, arXiv preprint arXiv:2406.12148 (2024).
- [36] N. I. Muskhelishvili, Some basic problems of the mathematical theory of elasticity, 4th Edition, Cambridge University Press, Cambridge, 1966.
- [37] K. Amano, A charge simulation method for the numerical conformal mapping of interior, exterior and doubly-connected domains, *J. Comput. Appl. Math.* 53 (3) (1994) 353–370.
- [38] K. Sakakibara, Bidirectional numerical conformal mapping based on the dipole simulation method, *Eng. Anal. Bound. Elem.* 114 (2020) 45–57.
- [39] G. Exadaktylos, M. Stavropoulou, A closed-form elastic solution for stresses and displacements around tunnels, *Int. J. Rock Mech. Min. Sci.* 39 (7) (2002) 905–916.
- [40] Y. Ma, A. Lu, H. Cai, X. Zeng, Numerical applications of conformal mapping with explicit formulae based on the power series method, in: *Applied Mathematics, Modeling and Computer Simulation*, IOS Press, 2022, pp. 237–252.
- [41] Z. Ye, Z. Ai, A novel complex variable solution for the stress and displacement fields around a shallow non-circular tunnel, *Comput. Geotech.* 164 (2023) 105797.
- [42] D. Okano, H. Ogata, K. Amano, M. Sugihara, Numerical conformal mappings of bounded multiply connected domains by the charge simulation method, *J. Comput. Appl. Math.* 159 (1) (2003) 109–117.
- [43] D. M. Hough, N. Papamichael, The use of splines and singular functions in an integral equation method for conformal mapping, *Numer. Math.* 37 (1981) 133–147.
- [44] D. Hough, N. Papamichael, An integral equation method for the numerical conformal mapping of interior, exterior and doubly-connected domains, *Numer. Math.* 41 (1983) 287–307.